

Nanocomposite approach to couple Magnetic and Electric ordering



A thesis submitted towards the partial fulfilment of
BS-MS Dual Degree Programme

By

Swathi Krishna. S

(20131037)

Under the guidance of

Prof. Satishchandra B. Ogale

Professor

Indian Institute of Science Education and Research (IISER)

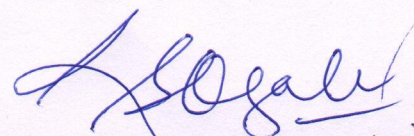
Pune

Certificate

This is to certify that this dissertation entitled "*Nanocomposite approach to couple magnetic and electric ordering*" towards the partial fulfillment of the BS-MS dual degree programme at the Indian Institute of Science Education and Research, Pune represents study/work carried out by **Swathi Krishna. S** at IISER Pune under the supervision of **Prof. Satishchandra B Ogale**, Professor, Department of Physics during the academic year 2017-2018.

Swathi Krishna. S

Registration Number: 20131037



Prof. Satishchandra B Ogale

Professor

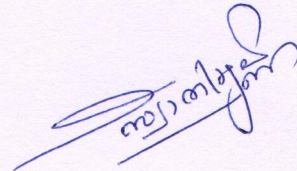
Committee:

Prof. Satishchandra B. Ogale (supervisor)

Dr. Ashna Bajpai (TAC)

Declaration

I hereby declare that the matter embodied in the report entitled "*Nanocomposite approach to couple electric and magnetic ordering*" are the results of the work carried out by me at the Department of Physics, IISER Pune, under the supervision of Prof. Satishchandra B. Ogale and the same has not been submitted elsewhere for any other degree.



Swathi Krishna. S

Registration Number: 20131037

Dedicated to my beloved parents

Acknowledgement

I express my heartfelt respect and gratitude to my mentor Prof. Satishchandra B. Ogale for his excellent mentorship, immense knowledge, continuous support and encouragement throughout the duration of my research period. I specially thank Dr. Smita Chaturvedi for guiding me well through this project. Her constant support and valuable suggestions helped me overcome all the difficulties and making things happen. I realize that these words are not enough to acknowledge her, but still I would like to express my heartfelt gratitude to her. I would also like to thank my lab members for creating a lively lab atmosphere, their continuous co-operation and stimulating discussions.

I thank Mr. Yathish and Mr. Anil Prathamshetti for helping me in acquiring all the FESEM data. I would also like to thank Priyank for helping me with the refinement part of XRD. I express my gratitude to Vijayakanth and Dr. Bhoomishankar for helping me in acquiring P – E loop measurements. I also thank Dr. R.J Choudhary, UGC-DAE-CSR, Indore for the magnetic measurements (M – H loop). I am grateful to Department of Science and Technology (DST), for the INSPIRE fellowship programme for their incessant support. I also extend my gratitude to the rest of administrative and non-administrative staff at IISER Pune who have directly or indirectly helped me with the project.

I specially thank my family, Achan and Amma for their unconditional love, care and support without them this work would not have been successful. I am indebted to my dearest friends Athul, Jithin, Anjana, Alma, Swetha, Rintu and Devika for their tremendous help and support.

Finally, I thank God almighty for being with me all the time.

Contents

1. Introduction

1.1 Magnetolectric Multiferroics.....	7
1.1.1 History of multiferroics.....	7
1.1.2 Physical and mathematical background.....	8
1.1.2.1 Type I Multiferroics.....	10
1.1.2.2 Type II Multiferroics.....	11
1.1.2.3 Magnetolectric coupling.....	12
1.1.3 Applications.....	13
1.2 Why nanocomposite approach?.....	13
1.3 Why RFeO ₃ based nanostructures?.....	14
1.4 Selection of materials.....	15
1.4.1 LuFeO ₃	15
1.4.2 HoFeO ₃	16
1.4.3 BiFeO ₃	16
1.4.4 BaTiO ₃	16
1.5 Summary.....	17

2. Experimental Section

2.1 Synthesis of nanofibers.....	19
2.1.1 Electrospinning.....	19
2.1.2 Materials.....	21

2.1.3 Synthesis of LuFeO ₃ (LFO) Nanofibers.....	21
2.1.4 Synthesis of HoFeO ₃ (LFO) Nanofibers.....	21
2.1.5 Synthesis of BiFeO ₃ (BFO) Nanofibers.....	22
2.1.6 Synthesis of BaTiO ₃ (BTO) Nanofibers.....	22
2.1.7 Synthesis of HFO-BTO Composite Nanofibers.....	22
2.1.8 Synthesis of HFO-BTO Heterostructure Nanofibers.....	23
2.2 Analysis Techniques.....	23
2.2.1 Field Emission Electron Microscopy (FESEM).....	23
2.2.2 Energy Dispersive X-ray Analysis (EDX).....	24
2.2.3 Powder X-ray Diffraction (XRD).....	25
2.2.4 Raman Spectroscopy.....	26
2.2.5 M – E loop measurements.....	28
2.2.6 P – E loop measurements.....	29

3. Results and Discussion

3.1 LuFeO ₃ Nanofibers (LFO NF).....	30
3.1.1 Morphology.....	30
3.1.2 Structure.....	31
3.2 HoFeO ₃ Nanofibers (LFO NF).....	35
3.2.1 Morphology.....	35
3.2.2 Structure.....	36
3.3 BiFeO ₃ Nanofibers (BFO NF).....	38
3.3.1 Morphology.....	38
3.3.2 Structure.....	39

3.4 BaTiO ₃ Nanofibers (BTO NF).....	41
3.4.1 Morphology.....	41
3.4.2 Structure.....	42
3.5 Composite and Heterostructure.....	44
3.5.1 FESEM.....	44
3.5.2 XRD.....	47
3.5.3 Raman.....	50
3.5.4 Physical property measurements.....	51
3.6 Concluding Remarks.....	53
4. Summary and future directions.....	54
4.1 What was achieved?	54
4.2 What next?	55
Bibliography.....	56

List of Figures

1.1 Multiferroics and magnetoelectric incomplete overlap.....	8
1.2 Time reversal and spatial inversion symmetry for ferroics.....	9
1.3 Schematic of interaction between different degrees of freedom.....	14
1.4 Structural transition in BaTiO ₃ with temperature.....	17
2.1 A typical Electrospinning set up.....	20
2.2. Schematic on working of FESEM set up and principle behind EDAX.....	23
2.3 Bragg's Diffraction principle and schematic on working of X-ray Diffractometer.....	26
2.4 Energy level diagram for Raman scattering and schematic of Raman Spectrometer.....	27
2.5 Schematic of Vibrational Sample Magnetometer and Sawyer-Tower circuit.....	28
3.1 FESEM images and EDAX spectra of LFO NFs.....	31
3.2 XRD pattern of LFO NFs.....	32
3.3 Raman spectrum for LFO NFs and HFO NFs.....	33
3.4 FESEM images and EDAX spectra of HFO NFs.....	35
3.5 XRD pattern of HFO NFs.....	36
3.6 FESEM images and EDAX spectra of BFO NFs.....	38
3.7 XRD pattern of BFO NFs.....	39
3.8 Raman spectrum for HFO NFs and BFO NFs.....	41
3.9 FESEM images and EDAX spectra of BTO NFs.....	42
3.10 XRD pattern of BTO NFs.....	43
3.11 FESEM images and EDAX spectra of composite NFs.....	45
3.12 FESEM images and EDAX spectra of heterostructure NFs.....	46
3.13 XRD pattern of composite and heterostructure.....	47
3.14 Rietveld refinement results for heterostructure.....	48
3.15 Distortion of TiO ₆ octahedra	49
3.16 Raman spectra for composite and heterostructure.....	50

3.17 M-H loop measurements.....	51
3.18 P-E loop measurements.....	52

List of Tables

3.1 Unit cell parameters calculated for Nanofibers.....	33
3.2 Reported Raman modes and experimental value of LFO NFs.....	34
3.3 Reported Raman modes and experimental value of HFO NFs	37
3.4 Reported Raman modes and experimental value of BFO NFs	40
3.5 Reported Raman modes and experimental value of BTO NFs	43
3.6 Experimentally obtained values of composite and heterostructure.....	51

Abbreviations

LuFeO ₃ , Lutetium Ferrite	LFO
HoFeO ₃ , Holmium Ferrite	HFO
BiFeO ₃ , Bismuth Ferrite	BFO
BaTiO ₃ , Barium Titanate	BTO
RFeO ₃ , Rare earth orthoferrite	RFO
Magnetoelectric	ME
Multiferroic	MF
Field Emission electron microscopy	FESEM
Energy Dispersive X-ray Analysis	EDAX/EDX
X-ray Diffraction	XRD
Vibrating Sample Magnetometer	VSM
Nanofibers	NFs

Abstract

Multiferroic materials with co-existence of two or more ferroic orders hold utmost significance for the multifunctional device application, especially for data storage. Combining a ferromagnetic material with a ferroelectric material at nanoscale is one of the promising approaches to achieve multiferroicity. The reduction of the materials size to nanometer range brings out the quantum mechanical effect that impact the physical properties especially electron transport mechanism. Nanofibers due to their higher aspect ratio among the nonmaterial are interesting candidates and are considered for present study.

Present work focuses on the nanocomposite approach to bring out a material with magnetic and electric ordering. The nanofibers of certain rare earth orthoferrites (LuFeO_3 and HoFeO_3), known multiferroic BiFeO_3 and established ferroelectric BaTiO_3 were prepared using electrospinning a fiber fabrication technique. The prepared samples were characterized by scanning electron microscopy, powder X-ray diffraction and Raman spectroscopy. Among the prepared sample HoFeO_3 with Ho of highest magnetic moment of $10 \mu_B$ were chosen as magnetic parent compound and combined with ferroelectric BaTiO_3 to make composite. The composite and heterostructure were further characterized by XRD, Reitveld refinement, detailed deconvoluted Raman spectra with assignments of modes in detail. The analysis revealed that the Composite incorporates HoFeO_3 and BaTiO_3 in 54% and 46% respectively and in heterostructure it is 30% and 70% for HoFeO_3 and BaTiO_3 respectively. The Ti shift in the TiO_6 octahedra of composite and heterostructure compared to uncoupled BTO shows that the incorporation of HFO resulted in the distortion of the structure. The M – H loop and P – E loop confirms the ferroelectric and magnetic ordering of prepared samples.

Chapter 1

Introduction

1.1 Magnetoelectric Multiferroics

1.1.1 History of multiferroics

Magnetoelectric (ME) multiferroic (MF) materials where the magnetic and ferroelectric order coexist provides an excellent pathway to probe the functionalities of both the orders. The linear coupling between the two orders allows the control of magnetization by an electric field and vice versa, which makes them potential candidates for data storage, magneto-electric devices, magnetic switches, sensors and fuel cells.^[1] The term “magnetoelectric materials” was pointed out in Landau & Lifshitz^[2] *Electrodynamics of continuous media*, as “..... *The other is a linear coupling between magnetic and electric fields in media which would cause, for example, a magnetization proportional to an electric field.....*” which was predicted by Dzyaloshinskii and observed by D. Astrov in Cr_2O_3 .^[3]

Later, the term ‘magnetoelectric multiferroics’ was first used by H.Schmid during 1993 in MEIPIC conference of magnetoelectric and the emergence of the field, multiferroics were initiated by the paper published in 2000 “*Why are there so few magnetic ferroelectrics?*”^[4] by N.A Spaldin. It explained about the chemical and physical incompatibility for the existence of magnetic and ferroelectric order in single phase materials and various routes by which multiferroicity can be achieved in materials. This stimulated the scientific community and led to the extensive study in this area. The early works include the discovery of strong ferroelectric response in epitaxially grown BiFeO_3 thin films which is already ferromagnetic,^[1] observations of improper ferroelectricity with the co-existence of magnetism in h-YMnO_3 ,^[5] spin structure induced ferroelectricity observed in o-TbMnO_3 ^[6] and TbMn_2O_5 .^[6] These works attracted a group of scientists from different fields like material physics, condensed matter physics etc. that

resulted in the development of multiple materials that showed multiferroicity and their realization as devices.

The present work is primarily focused on the nanocomposite approach to achieve magnetic and electric ordering with rare-earth orthoferrites. The magnetic ordering and “4f-3d dynamics” which is the interplay between the 3d spins of transition metal and 4f moment of rare-earth element make these materials potential candidates for achieving multiferroicity.^[7] So, making composites using these materials with a known ferroelectric appears to be a promising method for obtaining magnetoelectric coupling. Herein, as well as in the subsequent chapters, the work done on the synthesis and properties of prepared materials and composites are described.

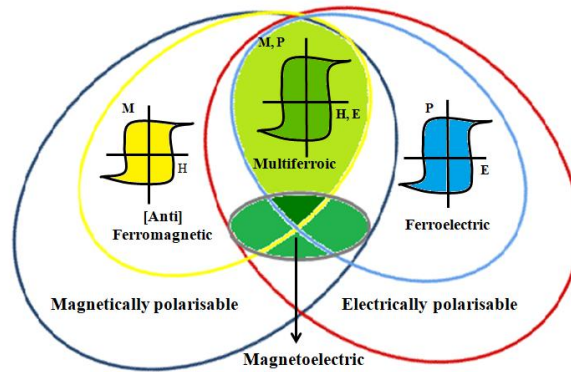


Figure 1.1: Multiferroics and magnetoelectric incomplete overlap

1.1.2 Physical and Mathematical Background

Multiferroics are ideally the materials with the presence of more than one primary ferroic orders like ferromagnetism, ferroelectricity and ferroelasticity in a single phase material with coupling between them. But most of the research is focused on magnetoelectric multiferroics (Figure.1) which is considered as an intriguing area because of the interesting physics as well the potential application in various fields such as magnetic field sensors, transducers, spintronics, effective and efficient data storage technologies. So far not many of such systems with the coexistence of these two orders with strong coupling between them at room temperature are known. In 2000, the review by Spaldin provided the reasons for the scarce of such materials with the versatile

perovskite structure which has technological importance.^[4] The reasons were presented from different perspectives like symmetry requirements, electric properties and the chemical structure which are as follows:

a) Symmetry

Considering the symmetry requirements, ferroelectric materials which have local dipole moment lying asymmetrically within the unit cell has broken spatial inversion and is invariant under time reversal. But for a ferromagnet, the magnetic moment arises due to the rotation of charge around an orbit, so the dynamics demand the breaking of time symmetry and invariant spatial symmetry. So a multiferroic with both ferroelectric and magnetic ordering possess neither of the symmetries. (Figure. 2)

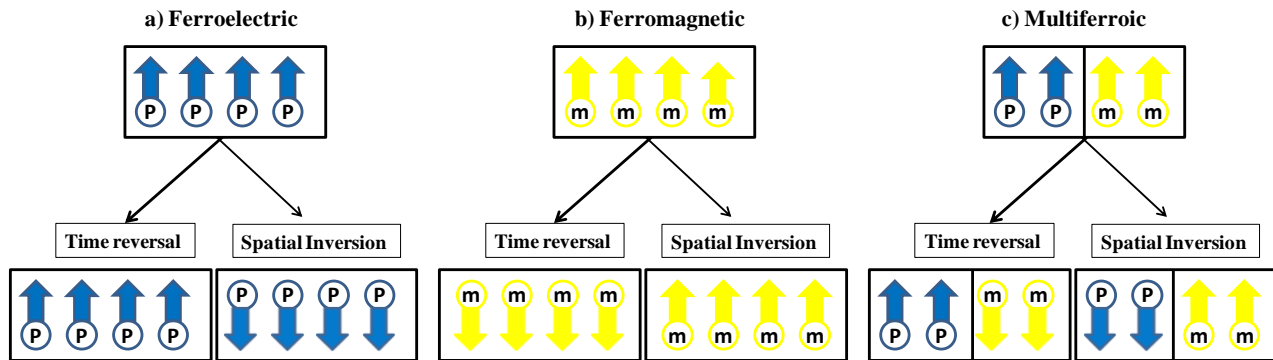


Figure 1.2: Time reversal and spatial inversion symmetries for ferroics.

b) Electric properties

Usually ferroelectric materials are insulators, because if they are metals, the applied electric field will result in electric current production rather than generating an electric polarization. But most of the ferromagnets are compounds of transition metals which have highly populated Fermi level and hence demonstrate metallic nature. The scarcity of magnetic insulators can also be a contributing factor for the rareness of multiferroics.

c) Chemistry: “ $d^0 - d^n$ dilemma”

In ABO_3 type structures the center atom with empty d-shell (d^0 -ness) hybridizes with electron cloud of oxygen octahedra, supporting the displacement of center atom and resulting in a net dipole moment. But in contrast for the existence of magnetism the 3d- shell should be half filled or partially filled (d^n -ness) rather than being empty. This is called as the “ $d^0 - d^n$ dilemma” which caused an increased pace in search for materials with nondisplacive ferroelectricity which permits the coexistence of magnetism and ferroelectricity.

Based on the origin of ferroelectricity multiferroic materials are been classified into two which are type I and type II multiferroics.^[8]

1.1.2.1 Type I Multiferroics

Type I multiferroics are those materials which have magnetic and ferroelectric orders of different origin, which are independent of each other or in other words a weak coupling between the orders. In such material both the electric and magnetic transition occurs at a temperature greater than room temperature but the weak coupling between the two orders make them unsuitable for the potential application, so most of the research on these materials is focused to increase the coupling between them. Depending on the origin of ferroelectricity in these materials they can be divided into subclasses, among them the major three are described below:^[9]

a) Ferroelectricity due to charge ordering

This occurs mostly in materials containing transition metals with different valencies. The valence electrons that are localized at higher temperature become localized non-uniformly, forming superstructures which give rise to definite polarization. The primary example of such a system is LuFe_2O_4 with Fe^{2+} and Fe^{3+} states forming super lattices and charge ordering occurs at 330 K.

b) Ferroelectricity due to lone-pairs

In such system the two outer 6s electrons of A-site cation do not take part in any sp-hybridization and act as lone pairs, but they share these electrons with formally empty p orbits of A-site element causing a polarization. The magnetization in these materials arises from the partially filled d-orbitals of B-site cation. The foremost example for such type of mechanism is BiFeO_3 ,

which is one of the most studied multiferroic till now. In BiFeO_3 the lone pairs in Bi^{3+} creates a local dipole and Fe^{3+} is responsible for the weak antiferromagnetism observed in it. This is the only material in lone-pair mechanism classification showing room temperature multiferroism in single phase with $T_C = 1103 \text{ K}$ and $T_N = 643 \text{ K}$.^[1]

c) Geometric Ferroelectricity

In geometric ferroelectric system, rather than electron sharing covalent bond formation the structural distortion of oxygen polyhedral around the small A-site cation results in polarization. Mostly the tilting of these polyhedra occurs due to close packing or geometric constraints. For example, in $h\text{-RMnO}_3$ (R: Ho-Lu, Y) the MnO_5 bipyramid tilting give rise to ferroelectric polarization.

1.1.2.2 Type II Multiferroics

The second class of multiferroics is essentially called as “Type II multiferroics” which is relatively new and the origin of ferroelectric polarization in such materials is the magnetism. This suggests that there is strong coupling between the two orders and it overcomes the problem with Type I. These materials also have certain drawback, such as smaller electric polarization values compared to Type I, which are very good ferroelectrics. Based on the magnetic ordering they are also classified into subclasses which are:

a) Spiral Type II Multiferroics

These are materials in which the magnetic structure is noncollinear, usually spiral or cycloids with considerable spin-orbit coupling. Example for such a system is TbMnO_3 .

b) Type II Multiferroics with collinear magnetic structure

In these materials the magnetic ordering is associated with symmetry breaking and this leads to the polarization. Example includes $\text{Ca}_3\text{CoMnO}_6$.

1.1.2.3 Magnetoelectric coupling

The magnetoelectric coupling effect in a single phase multiferroic system is given by Landau theory, in which the Landau Free Energy of the system is written in terms of E_i and H_i , the i th

component of \mathbf{E} and \mathbf{H} respectively.^[10] Using Einstein summation convention F for a material with ferroic orders is given as:

$$-F(E, H) = -F_o + P_i E_i + M_i H_i + \frac{1}{2} \varepsilon_0 \varepsilon_{ij} E_i E_j + \frac{1}{2} \mu_0 \mu_{ij} H_i H_j + \alpha_{ij} E_i H_j + \frac{\beta_{ijk}}{2} E_i H_j H_k + \frac{\gamma_{ijk}}{2} H_i E_j E_k + \dots \quad (1)$$

Where α is the linear magnetoelectric coefficient; β , γ are the coefficient of higher order terms of magnetoelectric coupling and ε_{ij} and μ_{ij} are the relative permittivity and permeability of the medium respectively. For a non-ferroic material where both the temperature dependent magnetization $M_i(T)$ and electric polarization $P_i(T)$ are both zero in the absence of an applied field, the equation reduces to:

$$-F(E, H) = +\frac{1}{2} \varepsilon_0 \varepsilon_{ij} E_i E_j + \frac{1}{2} \mu_0 \mu_{ij} H_i H_j + \alpha_{ij} E_i H_j + \frac{\beta_{ijk}}{2} E_i H_j H_k + \frac{\gamma_{ijk}}{2} H_i E_j E_k + \dots \quad (2)$$

The first term on the right hand side represents the electric response to the electric field E_i applied and the second term is the magnetic equivalence of it. The third term describes the linear magnetoelectric coupling and the terms with β_{ijk} , γ_{ijk} as coefficients represents the higher order terms of the magnetoelectric coupling.

The magnetoelectric effect can also be visualized in terms of resultants rather than applied fields. So the same equation can be obtained in terms of $P_i(H_j)$ and $M_i(P_j)$ by differentiating the equation (2) with E_i and putting $E_i=0$ for the former and the same process with H_i for the latter. The obtained are as follows:

$$P_i = \alpha_{ij} H_j + \frac{\beta_{ijk}}{2} H_j H_k + \dots \quad (3)$$

$$\mu_0 M_i = \alpha_{ij} E_j + \frac{\gamma_{ijk}}{2} E_j E_k + \dots \quad (4)$$

From equation (3) and (4) the α_{ij} can be interpreted as the control polarization by magnetic field or magnetization by an electric field. The sum of the first three terms equated to zero by ignoring the higher order terms gives the limiting condition for α_{ij} which is,^[11]

$$\alpha_{ij}^2 \leq \epsilon_0 \mu_0 \epsilon_{ij} \mu_{ij} \quad (5)$$

This provides a direct sense, why multiferroics have a large linear magnetoelectric coupling because they usually have (not always) large permittivity (for ferroelectric ordering) and permeability (for ferromagnetic ordering).

1.1.3 Applications

Magnetoelectric multiferroics have various applications like magnetoelectric devices, transducers, sensors, data storage, and fuel cells etc.. Among them the most worked upon area is magnetic storage devices because there is a great need to store the data as efficiently as possible. In multiferroics, the presence of both magnetization and polarization increases the availability of degrees of freedom, where we can encode information in both magnetic states and electric states. The presence of two states in each allows the realization of four state memory in a single bit. If such a system with the coexistence two primary orders has coupling between the two orders, enables the control of spins using electric field and charges by the magnetic field, then the data can be written electrically and read magnetically.^[12] This incorporates the functional aspects of FeRAM, but nonvolatile and advantages of magnetic data storage without generating a large local field and thus lower energy consumption.

1.2 Why Nanocomposite approach?

During the early stages of research, single phase multiferroics with direct magnetoelectric coupling were the main focus of the scientific community. But till now such a system with strong ME coupling does not exist. Despite type II multiferroics showing a reasonable coupling, the smaller magnitude of ferroelectric polarization made them unsuitable for technological applications. So regardless of the compulsive physics and properties of these single phase materials, they became unattractive for technological application. Later, intensive researches by the scientific community lead to the development of “composite multiferroics”, which showed the properties of both parent compounds with additional degrees of freedom by coupling between their properties.^[13] Unlike single phase materials with an isotropic chemical composition, in composite materials, the two primary orders are physically separated. Because of this separation the ME coupling present in them is not direct but somewhat indirect where

magnetization (polarization) is not directly affected by the electric field (magnetic field). In composite multiferroics, the cross-interaction of the primary orders occurs via strain,^[14] the magnetization results in the deformation of the material which induces a strain in the polarization axis and causes electric polarization and vice versa:^[15]

$$ME_{H\ effect} = \frac{\text{magnetic}}{\text{mechanical}} \times \frac{\text{mechanical}}{\text{electrical}} \quad (6)$$

$$ME_{E\ effect} = \frac{\text{electric}}{\text{mechanical}} \times \frac{\text{mechanical}}{\text{magnetic}} \quad (7)$$

Composite materials naturally satisfy symmetric, electric and chemical requirements since the two orders are separated within the material. The studies conducted show that composites show strong ME coupling, several orders of magnitude larger than single phase materials at room temperature.^[16] So the composites are the promising candidates for fabrication of devices mainly for data storage.

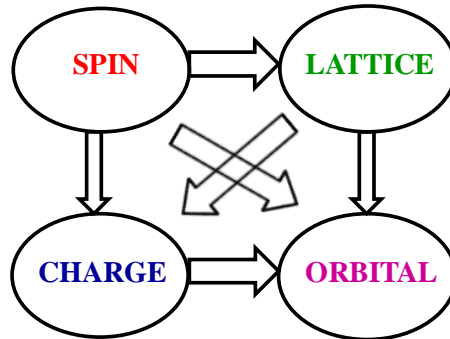


Figure 1.3: Schematic of interaction between different degrees of freedom

1.3 Why RFeO₃ based Nanostructures and composites?

RFeO₃ are materials with a perovskite-based structure where R= La – Lu which has been already exploited and established as one of the most promising materials for tailoring magnetic, electric properties including ferroelectricity as well as superconductivity, optical and mechanical properties. The crystal structure with the Fe metal at the center of the unit cell surrounded by six oxygen atoms sitting on the faces forms a FeO₆ octahedron that contributes much to these tunable properties. These materials are considered to be fruitful candidates for achieving multiferroicity because of the extraordinary physical phenomenon, arising from the interplay

between spin, lattice, charge and orbital degrees of freedom (Figure. 3). Most of the perovskite-based rare earth orthoferrites have structures which are distorted from the ideal cubic phase and the same structure with different materials show entirely different properties. The significant contributions to these properties arise from the interplay between the 3d orbitals (half filled) of Fe and 4f moments (half filled or partially filled) of the rare earth element.^[17] The strong exchange interaction between R and Fe make them promising candidates to achieve magnetic ordering and the easiness in tuning property made it considering for present work.

Nanostructures like nanotubes, nanofibers, nanoparticle, nanocomposite etc. have recently got great scientific attention due to its unique tunable properties. Among them, one dimensional structure like nanofiber and nanotubes appears to be interesting because of the unusual properties arising because of its confined structure which changes the electronic band distribution.^[18] When we reduce the length scale to nanometer range, the classical behaviour of the materials breaks down, and quantum effect becomes prominent and brings novel properties due to surface effects. Once the surface effects dominate it changes the electronic structure, domain switching and atom arrangement which will affect both the electric polarization and magnetization. Nanostructure magnetic materials are already established and well studied due to its size dependents effects in magnetic reversal, and they are also suitable for multiferroics because the high aspect ratio will bring strain mediated ME coupling.^[19]

1.4 Selection of materials

1.4.1 LuFeO₃

Among all rare earth orthoferrites LuFeO₃ is the one with smallest rare earth ion and thus showing large structural distortions^[20] is one of the emerging material in the arena of multiferroicity. It is found to be interesting because it exists in two structural forms, which are hexagonal and orthorhombic that significantly differ from each other in terms of the symmetry of the lattice. Recent studies in o-LuFeO₃ have shown that it exhibits room temperature multiferroicity of Type II with strong coupling between the orders. As mentioned earlier Type II multiferroics show magnetically driven ferroelectricity; In LuFeO₃ the non-collinear spin structure forming canted AFM (weak ferromagnetism, T_N=620K) leads to finite polarization, and this is mostly studied in bulk form.^[21] On the other hand h- LuFeO₃ which is a metastable state is

mostly studied in thin film form because it is stable only when structural strain is induced. The surprising fact about h- LuFeO_3 is that it also shows multiferroic property that too room temperature with an AFM ordering below $T_N = 440\text{K}$ in thin film form.^[22] So the idea of nanofibers of LuFeO_3 is novel and can bring interesting results.

1.4.2 HoFeO_3

This is one of the rare earth orthoferrite which shows fascinating phenomenon of spin reorientation of different ions at different temperatures. HoFeO_3 which crystallizes in orthorhombic structure (space group of Pbnm) orders antiferromagnetically at higher temperature ($T_N = 700\text{K}$). The canted AFM structure by the Fe^{3+} ions is responsible for the weakly ferromagnetic nature of this material, and it appears to be stable until 55K. Once it reaches 55K, the spin reorientation of Fe^{3+} happens, and the ordering disappears. But when the temperature goes below 35K the orientation of Ho^{3+} takes place resulting in distorted AFM ordering at about $T_N = 6.5\text{K}$. This is also important as Ho^{3+} has the largest ionic-magnetic moment of $10 \mu_B$ and it is less worked upon at nanoscale. So it will be interesting to study in nanofiber form and composite form.

1.4.3 BiFeO_3

Bismuth Ferrite is an established material in the arena of multiferroics since it is the only single phase material exhibiting multiferroicity at room temperature. This material has been widely studied over last few years. It shows ferroelectricity due to the lone pairs in Bi^{3+} ($T_C = 1103\text{K}$) and ferromagnetism due to the residual moment arising from the canted AFM structure ($T_N = 643\text{K}$).^[1] BFO has a rhombohedrally distorted structure with an excellent band gap of 2.3 eV which is suitable for absorbing visible range light and thus vital material for energy conversion. BFO nanofibers are also studied extensively for multiferroic^[23–25] as well as for photocatalytic activity.^[26,27]

1.4.4 BaTiO_3

Barium titanate is the first perovskite-based ferroelectric material with ferroelectric polarization at room temperature as well as above room temperature with a $T_C = 120^\circ\text{C}$.^[28] In BTO the ferroelectricity arises due to the displacement of Ti^{4+} ion along the c-axis which is coordinated

with surrounding six oxygen atoms. This material has already been realized in various electronic applications, and it is also important because it is a lead-free promising ferroelectric material. Another unique phenomenon observed in BTO is the structural transition happening below T_C . Above the Curie temperature it becomes paraelectric and stabilizes in cubic structure which is stable up to 1460°C , but below T_C there are various transitions starting from a paraelectric to ferroelectric at 120°C with structure changing to tetragonal. Later it undergoes the more structural transition at -50°C to orthorhombic and finally to rhombohedral structure at -90°C (Figure. 4).^[29]

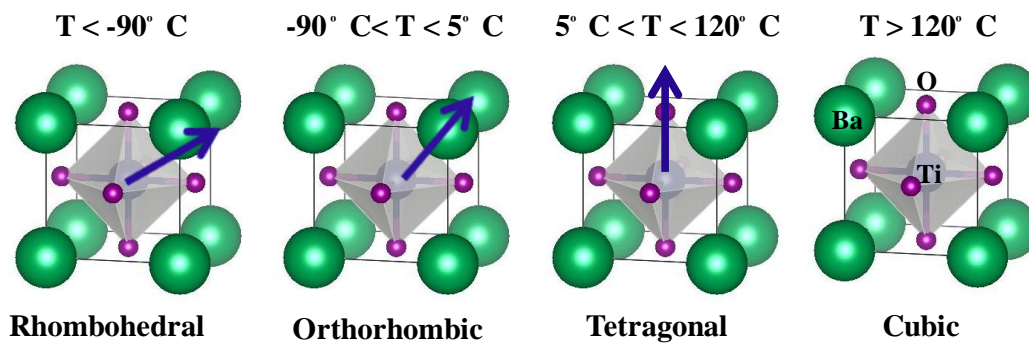


Figure 1.4: Structural transitions in BaTiO_3 with temperature

1.5 Summary

Magnetolectric multiferroics are one sought after research area, where the rapid pace of the research has resulted in the advancement of these materials in various application especially data storage. But the dearth of such single-phase materials due to physical and chemical incompatibility for the existence of two ferroic orders made these challenging. The theoretical correlated study on the origin the extraordinary phenomenon of coexistence revealed the condition necessary for that and concentrated efforts provided a variety of pathways to overcome this challenge. Among them, the most promising one was making composites of a ferroelectric and ferromagnetic material. It appeared to be attainable because it shows the properties of both parent compounds and strain mediated coupling between them results in ME coupling without much contradiction.

Once the ME coupling was achieved, there was a need for enhancing the coupling for technological application. There comes the importance of selection of materials and morphology of the materials. Rare earth orthoferrites with unique "4f-3d" dynamics were considered as parent compounds for magnetic origin because of two sources of magnetic ordering which are Fe and Rare earth ions. Combining this material with a well known ferroelectric material will incorporate the two orders in the materials and the coupling can be achieved and improved by reducing their dimension as well as the size of the particles to the nanometer scale. Once all these are achieved this can be harnessed into applications in electronic as well as data storage devices.

Chapter 2

Experimental Techniques

This chapter discusses the synthesis of nanofibers of perovskite-based materials including rare earth orthoferrites using electrospinning technique. The characterization and analysis techniques used for the experiment with a briefing of the fundamental principles involved in the techniques are discussed also discussed.

2.1 Synthesis of Nanofibers

We have used a versatile technique called Electrospinning for synthesizing Nanofibers.

2.1.1 Electrospinning

Electrospinning, an electric fiber fabrication technique is a unique and versatile approach to produce nanofibers and nanofabrics of wide applications ranging from tissue engineering to sensors. This spinning technique which is very robust and simple in procedure produces high-quality fibers of diameter ranging from nanometer to micrometer scale. The fiber obtained from this technique usually have a large surface to volume ratio, tunable porosity, malleability and easiness in manipulating the composition of the fibers.^[30] A typical setup of electrospinning includes three major components, a) high voltage supply (orders of tens of kV), b) a spinneret (for e.g.: A plastic syringe with needle) and c) a grounded collector which can be either rotating (Figure 5 (a)) or static collector (Figure 5 (b)).

During the electrospinning process, a polymer solution with optimized viscosity and concentration is loaded into a plastic syringe with a needle that acts as a capillary. A high voltage of the order of tens of kV is applied to the tip of the needle, and the polymer solution held by the surface tension at the tip acquires an electric charge due to the electric field developed. When the electric field crosses a critical value, the solution gets accelerated towards the collector of opposite polarity forming a cone called Taylor cone. Later the solution ejected from the cone gets elongated, forms fibers and gets deposited on the collector.

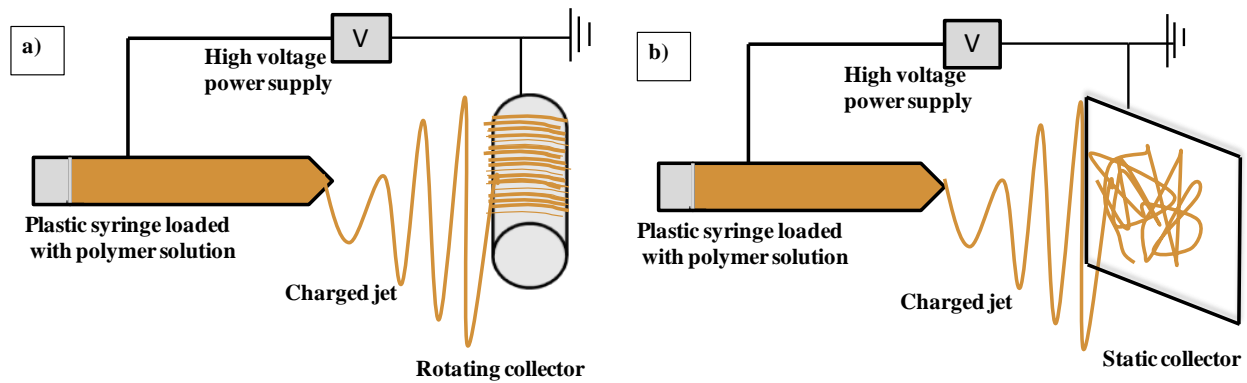


Figure 2.1: A typical Electrospinning set up a) Rotating collector b) static collector

The essential parameters that affect the fiber formation like voltage, flow rate, polymer concentration, etc. which are discussed below:

a) Polymer concentration – The viscosity of the solution which controls the fiber formation is dependent on the concentration of the polymer. An insufficient viscosity will hinder the fiber formation but if it is too high the formation of Taylor cone will be difficult and thus affects fiber formation.

b) Applied Voltage – Voltage is one of the critical factors deciding the quality of formed fibers. The fibers formation is only initiated when the threshold voltage is crossed. It is also noticed that with the increase of voltage the fiber diameter decreases because of the elongation and with low voltage fibers of larger diameter is formed.

c) Flow rate – This is the parameter which controls the jet velocity and material transfer and thus controls the quantitative properties of fibers like its composition which also depends on the prepared solution. It is desirable to keep low flow rate so that the solvent gets enough time for evaporation which could otherwise lead to beads formation.

d) Collector – There are two types of collectors, static and rotating. The former one gives randomly aligned fibers, and the latter gives aligned fibers. Usually, Aluminium foil is used as the collector.

e) Tip to collector distance – This parameter does not directly affect the morphology of the fibers, but a minimum distance should be maintained between the collector and needle tip so that

the solvent evaporates and continuous fibers are formed otherwise it will lead to beads formation.

The other factors that affect fiber formation are solution conductivity, ambient parameters like temperature, pressure, and humidity.

2.1.2 Materials

Holmium Nitrate Pentahydrate (($\text{Ho}(\text{NO}_3)_3 \cdot 5\text{H}_2\text{O}$), Alfa Aesar, 99.9 %), Lutetium Nitrate Hydrate (($\text{Lu}(\text{NO}_3)_3 \cdot \text{H}_2\text{O}$), Sigma Aldrich, 99.99%), Bismuth Nitrate Pentahydrate (($\text{Bi}(\text{NO}_3)_3 \cdot 5\text{H}_2\text{O}$), Merck, 98%), Barium Acetate (($\text{Ba}(\text{CH}_3\text{COO})_2$), Fisher Scientific, 99%) Polyvinylpyrrolidone ((PVP, MW: 1,30,000), Sigma Aldrich) Titanium Isopropoxide ($\text{Ti}\{\text{OCH}(\text{CH}_3)_2\}_4$), Iron Nitrate Nonahydrate (($\text{Fe}(\text{NO}_3)_3 \cdot 9\text{H}_2\text{O}$), Merck, 98%), Glacial acetic acid, Ethanol and Distilled Water.

2.1.3 Synthesis of LuFeO_3 (LFO) Nanofibers

The LuFeO_3 fibers were synthesized by sol-gel based electrospinning technique. The precursor solution was prepared by mixing $\text{Lu}(\text{NO}_3)_3 \cdot \text{H}_2\text{O}$ and $\text{Fe}(\text{NO}_3)_3 \cdot 9\text{H}_2\text{O}$ in 1:1 ratio (0.47M in 10 ml ethanol-water mixture) which was stirred for 30 minutes. This solution was mixed with Polyvinylpyrrolidone (1.4g) dissolved in 6ml ethanol (stirred for 12 hrs) and was stirred for 1 hour to optimize the viscosity and volatility. The prepared solution was loaded into plastic syringes with a needle. A grounded aluminum foil placed 12 cm away served as a counter electrode and collector plate. The nanofibers were made by applying a voltage of 22 kV to the solution through needle tip with a flow rate of 0.2ml/hr.^[31] The as-spun nanofibers were collected and dried at 120° C overnight and later annealed at 850° C (LFO 850) and 950° C (LFO 950) for 4 hrs. The fibers were grinded gently for obtaining fine powder.

2.1.4 Synthesis of HoFeO_3 (HFO) Nanofibers

The sol-gel solutions for HFO nanofiber preparation are as follows, the polymer PVP (1g) was dissolved in 6ml of ethanol and stirred for 2 hrs which were later mixed $\text{Ho}(\text{NO}_3)_3 \cdot 5\text{H}_2\text{O}$ and $\text{Fe}(\text{NO}_3)_3 \cdot 9\text{H}_2\text{O}$ in 1:1 molar ratio (0.39M) was prepared in 10 ml ethanol-water mixture. This solution was kept for 12 hrs stirring to obtain a homogeneous solution. The prepared solution was electrospun with a flow rate of 1 ml/hr by applying a voltage of 15 kV. The needle to tip

distance was fixed at 11 cm and used the rotating drum as the collector which was rotated at 800 rpm. The as-spun fibers went through a heating procedure by drying it at 120° C for 12 hrs and annealing at 800° C (HFO 800) and 850° C (HFO 850) for 3 hrs. After annealing, the obtained fibers were grinded.

2.1.5 Synthesis of BiFeO₃ (BFO) Nanofibers

Bi(NO₃)₃·5H₂O (0.8M) and Fe(NO₃)₃·9H₂O (0.8M) were dissolved in 2ml glacial acetic acid and stirred for 6 hrs. This was mixed with Polyvinylpyrrolidone (0.6g) dissolved in 3ml DI water and stirred for 12 hours to achieve the desired viscosity. The prepared solution was injected to the collector (12 cm apart) at a flow rate of 0.2 ml/hr.^[18] The nanofibers were made by applying a voltage of 15kV to the solution through needle tip, and a static collector was used for collecting the fibers. The as-spun nanofibers were collected and dried at 120° C overnight and annealed at 500° C for 4 hrs in air (BFO 500) and 700° C for 4 hrs in the argon atmosphere (BFO 700) which was grinded to obtain the powder.

2.1.6 Synthesis of BaTiO₃ (BTO) Nanofibers

BaTiO₃ fibers were prepared as follows. By sol-gel method 1.275g of Ba(CH₃COO)₂ was dissolved in 3ml of glacial acetic acid and stirred for 30 minutes. Later 1.475ml of Titanium Tetraisopropoxide was added dropwise to the above solution under constant stirring. This was mixed with PVP solution (0.2g in 3ml ethanol), stirred for 2 hours and the final solution was loaded into a 10ml plastic syringe.^[32] A positive terminal was connected to the needle tip and applied a voltage of 15 kV with aluminium foil as the counter electrode (rotating collector, 800 rpm speed) and electrospun with a flow rate of 1ml/hr. The distance between the needle tip and aluminum foil was fixed at 11 cm. The as-spun fibers were dried at 120° C for 12 hrs and annealed at 750° C (BTO 750) and 800° C (BTO 800) for 3 hours to obtain the final product.

2.1.7 Synthesis of HFO-BTO Composite Nanofibers

In this approach, the precursor solutions were prepared according to the previous sol-gel method used individually for HFO and BTO. The prepared solution was electrospun simultaneously placing the syringes in series but HFO and BTO needles kept alternatively. The solutions were loaded into plastic syringes with a stainless steel needle. The distance between needle tip and

collector was 11 cm; the voltage applied was 15 kV, and a flow rate of 0.8ml/hr. The as-spun fibers were collected on aluminium foil at rotating collector and dried at 120° C for 12 hrs followed by annealing at 800° C for 3 hrs.

2.1.8 Synthesis of HFO-BTO Heterostructure nanofibers

For heterostructures synthesis, the sol-gel solution preparation and electrospinning parameters were the same as that of composite synthesis. But instead of keeping the syringes of HFO and BTO solution simultaneously, they were placed alternately in a time gap of 1 hrs (spinning HFO solution for one hr followed by BTO and then again HFO forming the layered structure). The prepared sample went through the same heating procedure like 12 hrs drying at 120° C followed by annealing at 800° C for 3hrs.

2.2 Analysis Techniques

2.2.1 Field Emission Electron Microscopy (FESEM)

FESEM is an advanced microscopic technique using high energy electron beams for imaging. Compared to the conventional optical microscope using light for imaging FESEM provides high-resolution imaging. As the name suggests the electrons used for imaging is produced from a field emission source, and the produced electron beam is accelerated in high electric field gradient. A narrow beam of the primary electron is focused on the object and the bombardment of the electron beam with the objects produces secondary electron. A detector at high vacuum (10^{-7} torr) collects the secondary electron and process the signal to obtain high-quality scan image.^[33]

Rayleigh diffraction limits state that the resolution of the imaging system is limited by either aberration or diffraction which has a different origin. So by Rayleigh criterion the diffraction lower limit for spatial resolution in an optical microscope is around 200 nm whereas for an electron beam of $E= 5$ keV the wavelength can be can be calculated by wave-particle duality,

$$\lambda = \frac{h}{\sqrt{2mE}}$$

Where h is the Planck's constant and m is the electron rest mass. And the calculated de Broglie wavelength comes to be 0.017 nm which can be considered as the limit of resolution.

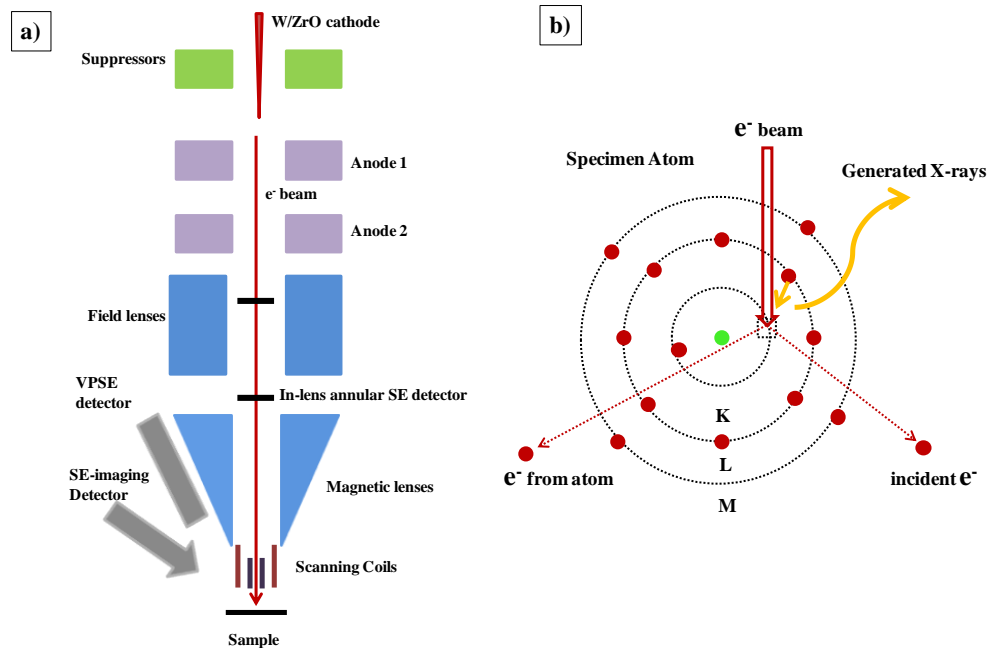


Figure 2.2: a) Schematic of Zeiss™ Ultra Plus FESEM b) Principle of EDX

This explicitly states that the electron microscope achieves higher spatial resolution compared to conventional optical microscopes. But the interaction of the object with the focused electron beam the secondary electrons will be slightly defocused resulting in lower resolution than expected. However, the electron beam can be focused into a small region of the sample by electrostatic lenses and practical resolutions for SEM ranges between 1-20 nm.

Samples which are fiber sheets were directly stuck to the carbon tape on the sample holder and directly did imaging without any coating since the sample was conducting. Figure 2.2 (a) shows the schematic of Zeiss™ Ultra Plus FESEM used for obtaining the high-resolution images of prepared samples. The thermal field emission source of the system is tungsten-zirconium oxide hybrid which operates between the voltage ranges of 2-40 kV. Electrostatic lenses are used for the precise focusing of the electron beam and the secondary electrons are collected using a detector at high vacuum.

2.2.2 Energy Dispersive X-ray Analysis (EDX)

Energy Dispersive X-ray Analysis (EDX) and elemental mapping were also done during the imaging for each sample in the same system. EDX is a technique used to confirm the elemental composition of the prepared sample by analyzing the energy of emitted X-ray during the process.

During the measurement, atoms are irradiated with high energy electrons which kick out the electron from the inner shells. Subsequently, electrons from the outer shell fall into this place taking that position. This process results in the reduction in the potential energy of the electron and thus emits X-ray whose energy is atom dependent (Figure 2.2 (b)). The detection of this X-ray helps to distinguish between the elements and its confirmation. The mapping of elements allows the visualization of the distribution of each element in the specimen by assigning different colours to each which is a qualitative analysis while EDX is quantitative.

2.2.3 Powder X-ray Diffraction

X-ray Diffraction (XRD) is one of the easiest and quickest ways to determine the crystal structure and its corresponding atom arrangement in materials. This technique involves the interaction of X-rays with sample and X-rays with X-rays itself, where the X-rays are produced by series of electron transition in specific target atoms usually Copper (Cu). When high energy electrons falls on the target atoms, the dislodging of electrons from the inner orbits (K-shell) occurs resulting in the replacement of electron from outer high energy shells (L and M). This energy difference results in the loosing of potential energy of electrons which are emitted as X-rays radiation namely $K\alpha$ and $K\beta$. The best diffraction patterns are obtained when continuous monochromatic X-rays are used, so the intense Cu- $K\alpha$ with $\lambda=0.1541$ nm is typically used.

The diffraction condition is explained in its simplest form by Bragg's Law of diffraction which relates the wavelength (λ) of the incident electromagnetic radiation to the diffraction angle (Θ) and the lattice spacing (d_{hkl}) given by:

$$n\lambda = 2d_{hkl}\sin\theta$$

Where n is an integer. According to this formula when a material is illuminated with an X-rays beam, the X-rays get reflected by the crystal plane, and each crystal plane deflects these rays at a particular Θ value. These deflected X-rays interact with each other resulting in constructive and destructive interference and causing a diffraction pattern. The Bragg's law essentially represents the condition for constructive interference which is depicted in Figure 2.3 (a).

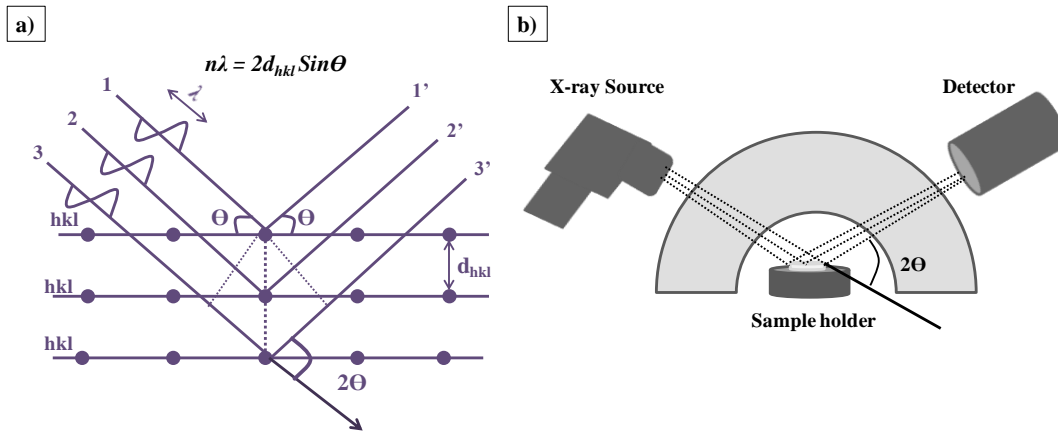


Figure 2.3: a) Bragg's Diffraction b) schematic of Bruker D8 Advance X-ray Diffractometer

The schematic of Bruker D8 Advance X-ray Diffractometer set up with Cu-K α radiation is shown in Figure 2.3 (b) which consists of an X-ray source equipped with a collimator, a sample holder, and an X-ray detector. During the measurements, only the source and detector move forming an angle with the sample which is kept in the fixed sample holder. For our measurements powder samples were spread uniformly over a glass slide, directly kept on the sample holder and was scanned from 10° to 80° with a step size of 0.01° and time per step of 2s/step. The grain size of the sample was calculated using Debye-Scherrer Formulae:

$$p = \frac{0.9\lambda}{\beta \cos\theta}$$

2.2.4 Raman Spectroscopy

This is a technique based on the Raman scattering (Raman Effect) discovered by Sir C. V. Raman in 1928 which is used to probe the rotational, vibrational and other lower frequency modes of molecules that help to study the molecular vibrations and crystal structure of the system. When the light scatters matter most of the light scattering back undergoes elastic scattering with no change in energy, and this is called Rayleigh scattering ($\nu_0 = \nu_1$). But a small amount of light undergoes inelastic scattering, with the scattered light having different energy than the incident light and this is called Raman Scattering. Based on the energy of the scattered light the Raman Scattering is classified into two; Stokes Raman Scattering and anti-Stokes Raman Scattering. Stokes Raman scattering is a process in which the electrons are excited from

the ground level and falls in to a vibrational level, thus the energy of the scattered light is lesser (longer wavelength) than the incident light ($\nu_0 > \nu_1$), Whereas in anti-Stokes scattering the reverse is true ($\nu_0 < \nu_1$) as shown in Figure 2.4 (a).

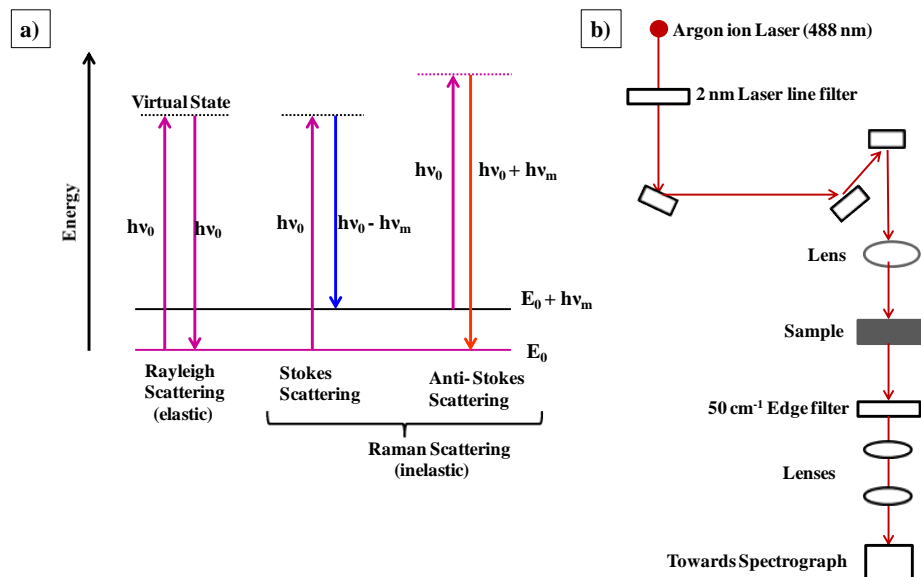


Figure 2.4: a) Energy-level diagram for Raman scattering b) Schematic of Horiba Jobin Yvon LabRAM HR Raman spectrometer

Compared to dominant Rayleigh scattering the intensity of Raman scattering is extremely weak (10^{-6} of incident beams). In Raman scattering also the intensity of Stokes and anti-Stokes depends on the population of different states in the system. Generally, at room temperature the ground state population will always be higher than vibrational states, so the intensity of Stokes Raman is greater than anti-Stokes. During this process, the electron cloud of the molecule is shifted to a virtual state which makes it different from absorption/ Fluorescence where the transition occurs between real states. The shift in the photon frequency during the transition ($\nu_0 - \nu_1$) is considered as the vibrational frequency.^[33]

The schematic of Horiba Jobin Yvon LabRAM HR Raman spectrometer is shown in Figure 2.4.b which consists of an Argon ion laser of wavelength 488 nm that is used for acquiring the spectra. The laser line is focused on the powder sample pressed uniformly in a glass slide by mirror based optics. The laser light transmitted from the sample is filtered using a 50cm⁻¹ edge filter to remove the Rayleigh scattering which is again passed through series of lens system for spectrograph analysis

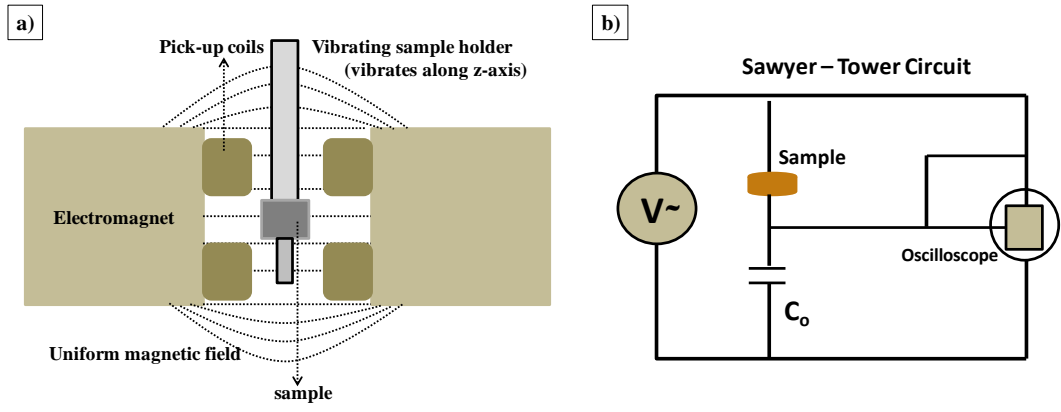


Figure 2.5 a) Typical VSM set-up b) Sawyer-Tower Circuit

2.2.5 M – H loop measurements

Vibrating Sample Magnetometer (VSM) is an instrument used for the measurement of magnetic properties of materials that work on the basis of Faraday's Law of Induction. In VSM, during measurements, the sample is placed in-between electromagnets that generate a constant uniform magnetic field. If it is a magnetic sample the generated field will cause the alignment of independent magnetic moments causing a magnetization and the magnetic dipole moment in the sample causes a magnetic field around the sample called **Stray Magnetic Field**. During this, the sample is vibrated vertically (along the z-axis) with a vibrating sample holder which results in an alternating magnetic field produced by the sample. According to Faraday's Laws of Induction, an alternating magnetic field generates an electric field, and these are sensed by the pickup coils equipped near the sample holder and later get processed as the magnetization of the sample to a particular applied field. Then the constant magnetic field is varied over a range, and corresponding magnetization measurements generates the M-H curve for the sample.

A typical set up of VSM is shown in Figure 2.5 (a); it contains an electromagnet (water cooled), Vibrating extitor attached to sample holder, pick-up coils, and Hall probe. Usually, the sample is vibrated using a piezoelectric material which undergoes a sinusoidal motion. The electric signal sensed by the pick-up coils is directly proportional to the magnetic field generated by the sample and thus proportional to the magnetization of the sample which helps in the precise measurement of the magnetic moment of the sample.

2.2.6 P – E loop measurements

P – E loop measurements are conducted for the identification of ferroelectric materials, which if ferroelectric would give a hysteresis loop when an electric field is applied. The ferroelectric tester uses the sawyer mode for ferroelectric measurements. It consists of Sawyer-Tower circuit (Figure 2.5 (b)) with high AC voltage supply and a sensor capacitor (C_o). The capacitor connected in series with sample act as a sensor because the voltage across the capacitor is proportional to the polarization of sample. Thus it measures the hysteresis loop as well as quantifies the saturation polarization (P_S) and coercive field (E_C). For the measurements, the prepared powder samples are to be made into a pellet of particular diameter and thickness and will be coated with silver paint on both sides for the establishment of top and bottom contact.

Chapter 3

Results and Discussion

This chapter discusses the structural and morphological characterization of all the nanofibers synthesized including the HFO-BTO composite and heterostructure. A discussion on physical property characterizations like magnetic and electric measurements for the composite and individual fibers (HFO and BTO for comparison) is also presented along with.

3.1 LuFeO₃ Nanofibers (LFO NF)

3.1.1 Morphology

The result obtained for the studies based on the morphology of the fibers using FESEM are presented in Figure 3.1. Figure 3.1 (a) – (c) is showing the images of fibers before annealing, annealed at 850° C (LFO 850) and 950° C (LFO 950) respectively. It is observed that as-synthesized fibers have a smooth surface owing to the amorphous nature of the PVP polymer (used while making sol-gel solutions) and they have an average diameter~ 190 nm. The fibers that are annealed at higher temperature show a different surface morphology, which is coarser and smaller in length. Figure 3.1 (b) shows the image of LFO 850 with an average diameter in the range of 85-90 nm, where the decrease in the diameter of the fiber is due to the polymer decomposition which leaves pores in the fibers and resulting in a coarser surface. A close observation of the LFO 850 fibers (shown as inset in Figure 3.1 (b)) show that they are made up of fine grains that are closely packed, self assembled and self arranged. While for LFO 950 the surface appears to be rather smoother than LFO 850 without grains and shows an average diameter of 120 nm but the length has considerably reduced to few micrometers. It is clear from the images that as the temperature increases the diameter of fibers decreases and the fibers become more fragile and they break into nanotubes. Even though there is a decrease in diameter of heat treated fibers compared to as-synthesized, the average diameter of LFO 950 is greater than that of LFO 850 because of the growth in constituent grain size due to increase in temperature.

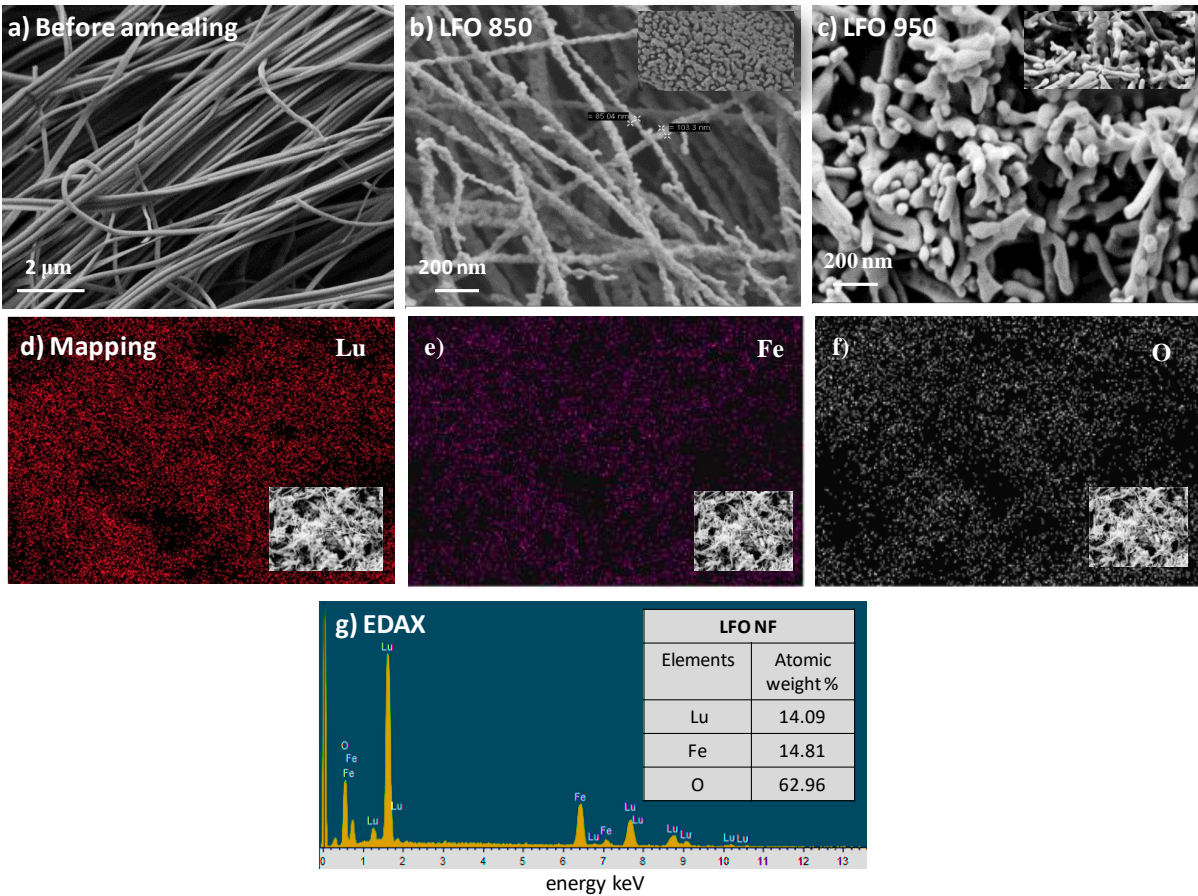


Figure 3.1: FESEM images and EDAX spectra of LFO NFs (a) before annealing, (b) LFO 850 (c) LFO 950 (d) – (f) Elemental mapping (g) EDAX spectrum (inset table shows elemental composition)

Figure 3.1 (d) shows the EDAX spectrum and its quantitative values obtained for annealed LFO fibers. It confirms that the ratio of Lu: Fe is maintained to be 1:1 and the qualitative analysis is represented in the form of elemental mapping (Figure 3.1 (e)) showing a uniform distribution over a region with fibers.

3.1.2 Structure

X-ray Diffraction and Raman spectroscopy were used for the structural analysis of the electrospun fibers. The XRD patterns observed for LFO 850 and LFO 950 are shown in Figure 3.2 (a) and 3.2 (b) respectively. LFO NFs that are annealed at 850° C shows a mixed phase of both orthorhombic and hexagonal structures which are significantly dissimilar in terms of symmetry of lattice as well as the surrounding of individual atom (Lu and Fe). Whereas for the

LFO 950 NFs, the XRD pattern is pure phase orthorhombic phase in good agreement with the JCPDS card No. 01-074-1957. The size of the grains in nanofibers calculated by Scherer formulae:

$$p = \frac{0.9 \lambda}{\beta \cos \theta}$$

(p = particle diameter, λ = wavelength of X rays used (1.54 Å), β = FWHM and θ is the Bragg's angle)

The particle size found to be 32.78 nm, for LFO 850 and 48.66 nm for LFO 950 which is in good agreement with increase in grain size observed by FESEM images. The unit cell parameters calculated for LFO 850 and LFO 950 is shown in Table 3.1, and it is observed that both show a volume compression compared to that of bulk (cell volume: 218.94) attributed to nano-structure size effect.

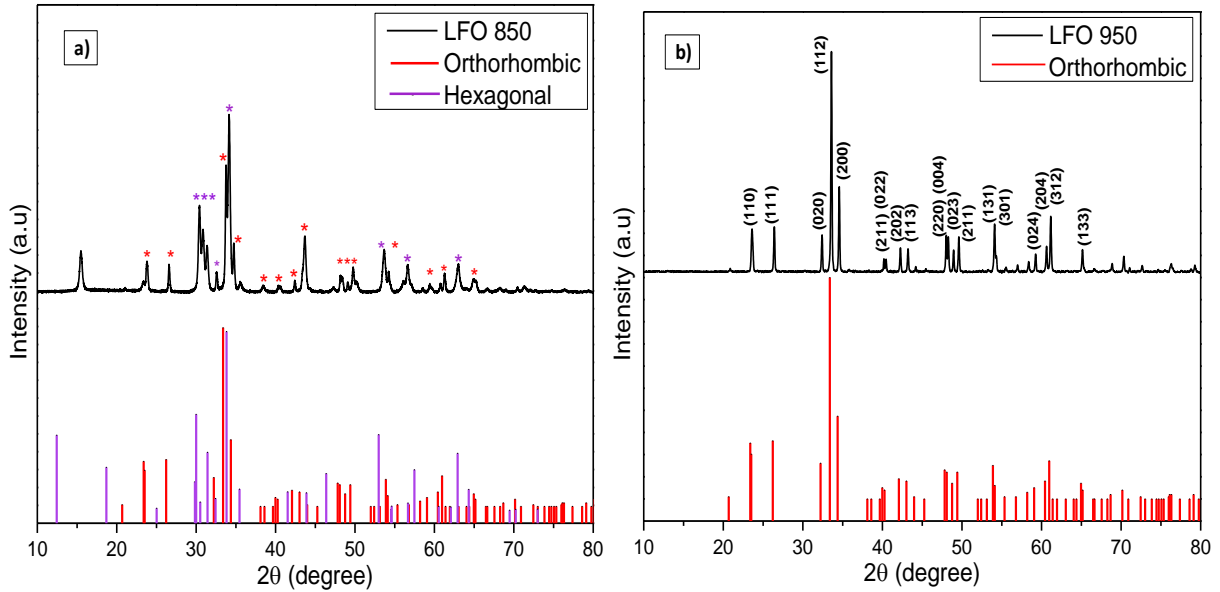


Figure 3.2: XRD pattern of LFO NFs (a) LFO 850 (mixed phase) (b) LFO 950 (pure phase)

Table 3.1: Unit cell parameters obtained for NFs

Parameters	LFO 850	LFO 950	HFO 800	HFO 850	BTO 750	BTO 800	BFO 500	BFO 700
a	5.23	5.18	5.19	5.25	3.98	3.96	3.95	3.93
b	5.30	5.52	5.50	5.55	---	---	---	---
c	7.36	7.51	7.51	7.53	3.98	---	---	---
Cell volume	204.50	214.99	214.57	219.82	63.13	62.30	185.16	183.28

Raman

Raman spectroscopy is a powerful technique to probe the structural properties by observing vibrational modes within the material. This technique also indicates the structural distortions, order-disorder effect and electric polarization. Figure 3.3 shows the room temperature Raman spectra obtained for LFO 850 (Figure 3.3 (a)) and HFO 800 (Figure 3.3(b)). LFO 850 is mixed phase with the co-existence of hexagonal and orthorhombic phases, shows Raman modes for both the phases as shown in Figure 3.3(a). The observed bands and assignment of peaks with reference to reported $R\text{FeO}_3$ and LuFeO_3 (hexagonal and orthorhombic phases separately) is given in table 3.2. The data show reasonable coherence with the reported values.

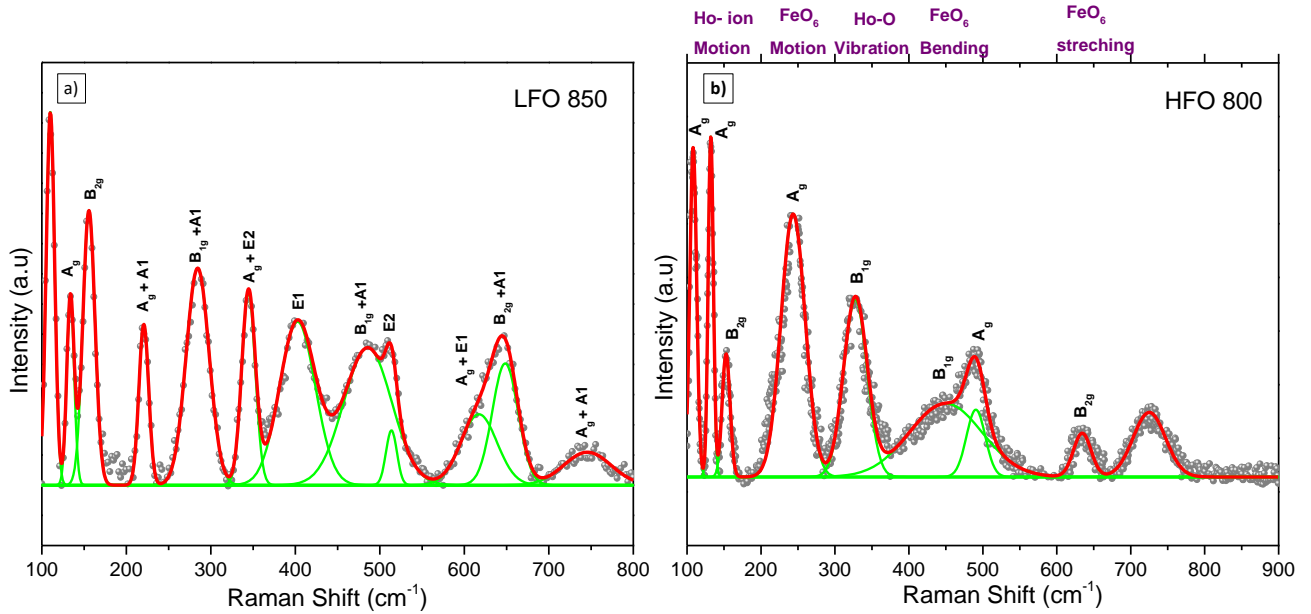


Figure 3.3: Raman spectra (a) LFO 850 (mixed phase) NF (b) HFO 800 (orthorhombic) NF

Table 3.2: Reported Raman modes and experimental values for LFO 850 (mixed phase) NFs

LFO (Orthorhombic)				LFO (Hexagonal)		LFO Nanofiber (mixed phase)
RFO ^[34]	Reported ^[35]	Modes	Attribute	Reported ^[36]	Modes	Present study
110	110	-	R- Motion	110	E2	110 - o
136	136	A_g	R- Motion	-	-	133 - o
160	158	B_{2g}	R- Motion	-	-	155- o
-	-	-		-	-	-
-	-	-		214	E2	-
225	-	A_g	FeO ₆ Rotation	223	A1	220- o, h
290	278	B_{1g}	FeO ₆ Rotation	289	A1	284 - o, h
349	350	A_g	R-O vibration	346	E2	344 - o, h
-	-	-		-	-	-
409	425	-	R-O vibration	404	E1	402 - o, h
-	-	-		-	-	-
-	-	-		-	-	-
428	427	A_g	FeO ₆ Rotation	448	E2	-
453	450	B_{1g}	FeO ₆ Rotation	473	A1	485 - o, h
517	516	-		501	E2	513 - o, h
608	-	A_g	FeO ₆ Rotation	603	E1	617- o, h
644	654	B_{2g}	FeO ₆ Rotation	651	A1	648 - o, h
		A_g	FeO ₆ Rotation	721	A1	745 - h

The data presented in the table 3.2 indicates that majority of the peaks observed for LFO 850 show the modes for orthorhombic^[34,35] and hexagonal^[36] phases. This is also confirmed by XRD.

The band peaks obtained at 110, 133, 155 cm^{-1} represent modes for orthorhombic phase (attributed to the rare earth ion motion) and mode at 745 cm^{-1} are from the hexagonal phase. The rest of all observed peaks show the mixed response of FeO_6 motion from orthorhombic phase and in plane and out of plane motion of atoms in the hexagonal phase.

3.2 HoFeO_3 Nanofibers (HFO NF)

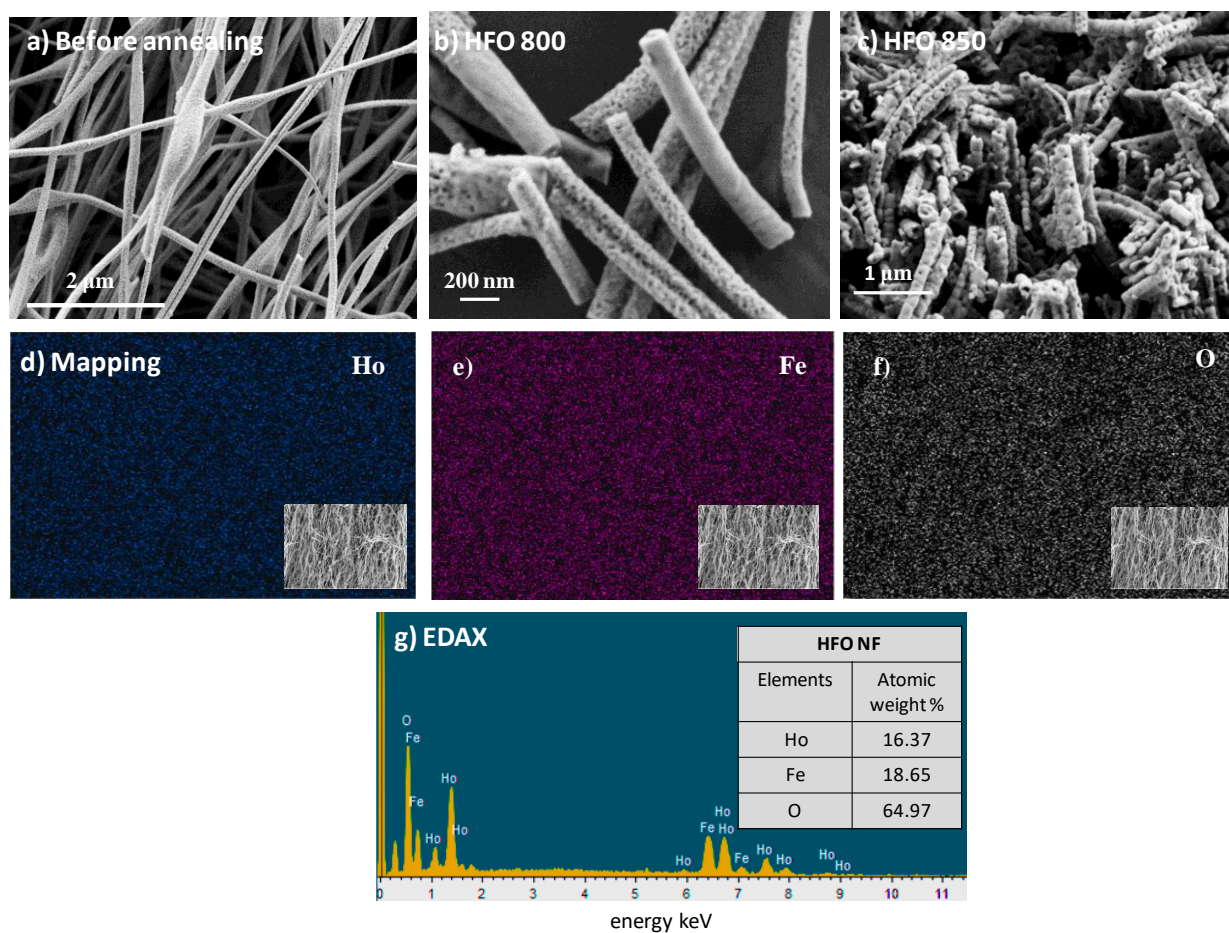


Figure 3.4: FESEM images and EDAX spectra of HFO NFs (a) before annealing, (b) HFO 800 (c) HFO 850 (d) – (g) Elemental mapping (h) EDAX spectrum (inset table shows elemental composition)

3.2.1 Morphology

Figure 3.4 (a) – (c) shows the FESEM images of HFO NF before annealing, annealed at 800°C (HFO 800) and at 850°C (HFO 850) respectively. As-synthesized and dried fibers of HFO have an average diameter of 240 nm with a smooth surface due to the presence of polymer. The fibers

that underwent a heat treatment show an average diameter of 156 nm and 190 nm for HFO 800 and HFO 850 respectively where the higher diameter of HFO 850 compared to HFO 800 is because of the increase in grain size. As discussed earlier the decrease in the diameter is because of the pyrolysis of polymer which makes the surface of fibers porous. It is clear from the images (Figure 3.4 (a) and 3.4 (b)) that as the temperature increases the fiber morphology is changing to nanotube structure due to the breakage of fibers, which has resulted in the considerable decrease in fiber length from 3-4 μm to 1-2 μm . So it is always desirable to anneal the fibers at low temperature which retains the fiber length and thus high aspect ratio. The elemental mapping shown in Figure 3.4 (d) shows that the elements are uniformly distributed in the fibers and the ratio is confirmed by the EDAX spectrum showing a ratio of 0.8: 1 for Ho: Fe.

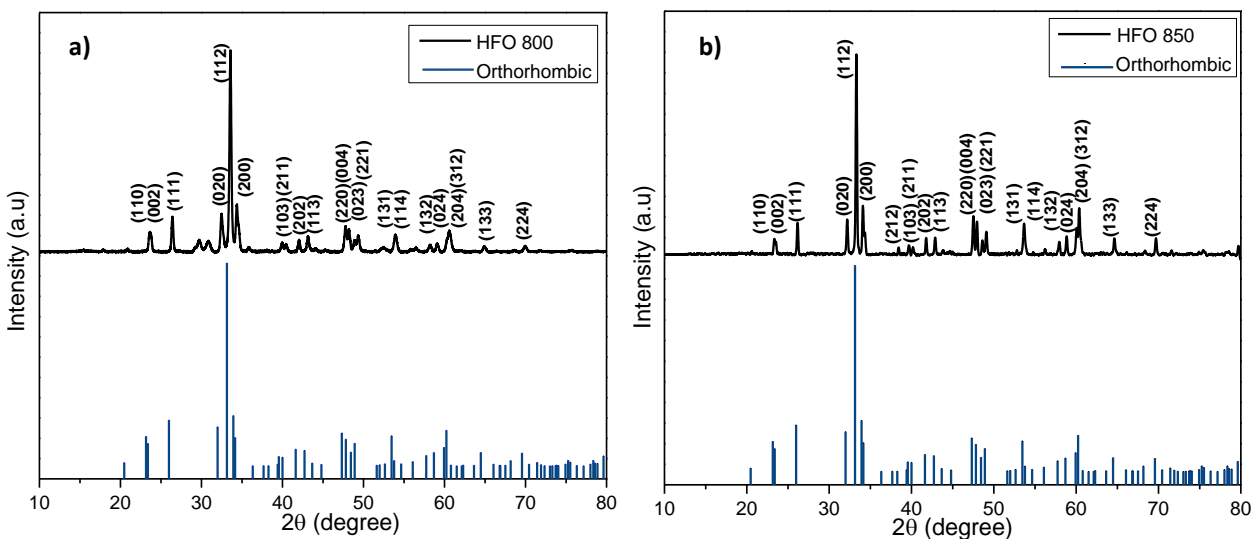


Figure 3.5: XRD patterns of HFO NFs (a) HFO 800 (b) HFO 850

3.2.2 Structure

The crystallinity and phase of the obtained fiber is confirmed with XRD patterns obtained shown in Figure 3.5 (a) and 3.5 (b) for HFO 800 and HFO 850 respectively. It is evident from the diffraction pattern that formed fibers are having orthorhombic crystal structure with space group of Pbnm matched with JCPDS-card no. 01-074-1479. HFO 800 shows small impurity peaks (due to small impurity of beta Fe_2O_3), which is removed on annealing at 850°C . From the obtained pattern the unit cell parameters a, b, c and cell volume were calculated for both HFO 800 and

HFO 850 which is given in Table 3.1 and it is observed that the cell volume for both is lesser than reported for bulk (224.33), caused because of the nanostructure effect. The size of the grains in nanofibers calculated by Scherer formulae, $p = 0.9\lambda/\beta\cos \Theta$ turned out be 28.63 nm for HFO 800 and 43.36 nm for HFO which is in good agreement with SEM images.

Table 3.3: Reported Raman modes and experimental values for HFO 800 NFs

HFO Nanofiber (orthorhombic)			
RFO ^[34]	Reported ^[37]	Modes	Present Study (HFO 800)
110	109	-	108
136	138	A_g	132
160	-	B_{2g}	152
-	-	-	-
-	-	-	-
225	-	A_g	237
290	270	B_{1g}	243
349	340	A_g	-
-	340	-	-
409	-	A_g	-
-	425	-	-
-	425	A_g	-
428	430	B_{1g}	-
453	-	B_{1g}	449
-	495	-	-
517	495	A_g	490
608	-	A_g	-
644	660	B_{2g}	634
-	-	-	725

Raman

Figure 3.3 (b) shows the Raman spectra of HFO NFs annealed at 800° C with orthorhombic crystal structure. The modes observed are compared with previously reported values for RFO^[34] and HFO^[37]. The modes obtained can be at a certain spectral range is assigned to specific symmetry operations which are as follows: (1) below 200cm⁻¹ that the lower wave modes are assigned to the rare earth ion Ho vibrations, (2) between 200 – 300cm⁻¹ – FeO₆ octahedral tilting, (3) 300 – 400 cm⁻¹ – vibration of R-O to be specific peaks at 349 and 409 cm⁻¹ (**A_g**) corresponds

to the Ho-O vibration, (4) 400 – 500 cm^{-1} the peaks are observed due to the FeO_6 bending motions and finally (5) above 500 cm^{-1} FeO_6 stretching modes. The experimentally observed modes of HFO NFs are close to the reported values.

3.3 BiFeO_3 Nanofibers (BFO NF)

3.3.1 Morphology

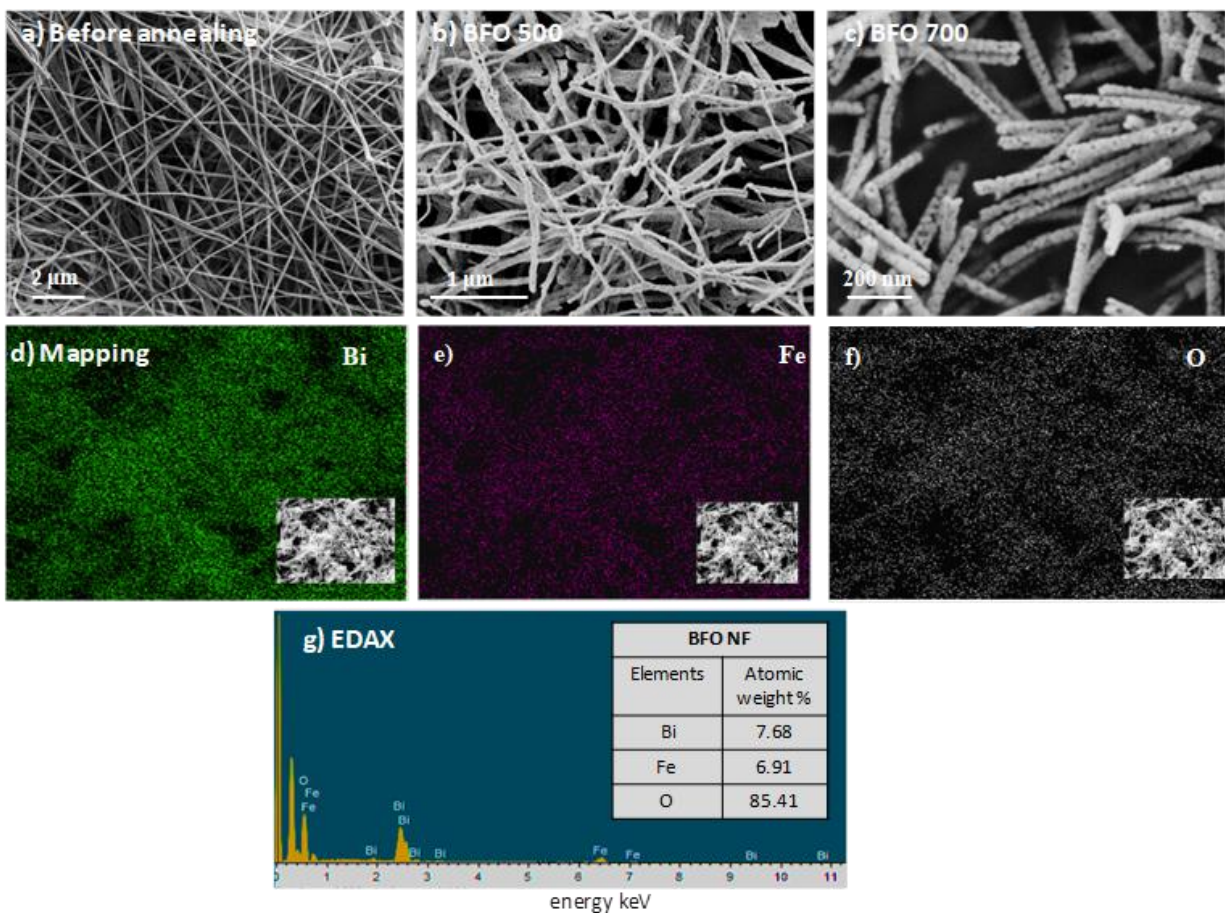


Figure 3.6 : FESEM images and EDAX spectra of BFO NFs (a) before annealing (b) BFO 500 annealed in air (c) BFO 700 annealed in argon (d) – (f) Elemental mapping (g) EDAX spectrum (inset table shows the elemental composition)

Figure 3.6 shows the FESEM analysis done for BFO NFs. The diameter of fibers before annealing is in the range of 150 – 200 nm (Figure 3.6 (a)), which decreases with the increase in the temperature to 160 nm for BFO 500 (annealed in air, Figure 3.3.b) and 105 nm for BFO 700 (annealed in argon, Figure 3.6 (c)). BFO 500 nanofibers despite showing porosity and

microstructure are not as smooth and self assembled as in BFO 700 which confirms that the optimum condition for high quality fiber is annealing at high temperature under inert atmosphere. From the EDAX analysis shown in Figure 3.6 (e), the calculated atomic ratio of Bi: Fe is almost 1: 1 and the uniform distribution of elements is shown in the elemental mapping given as Figure 3.6 (d).

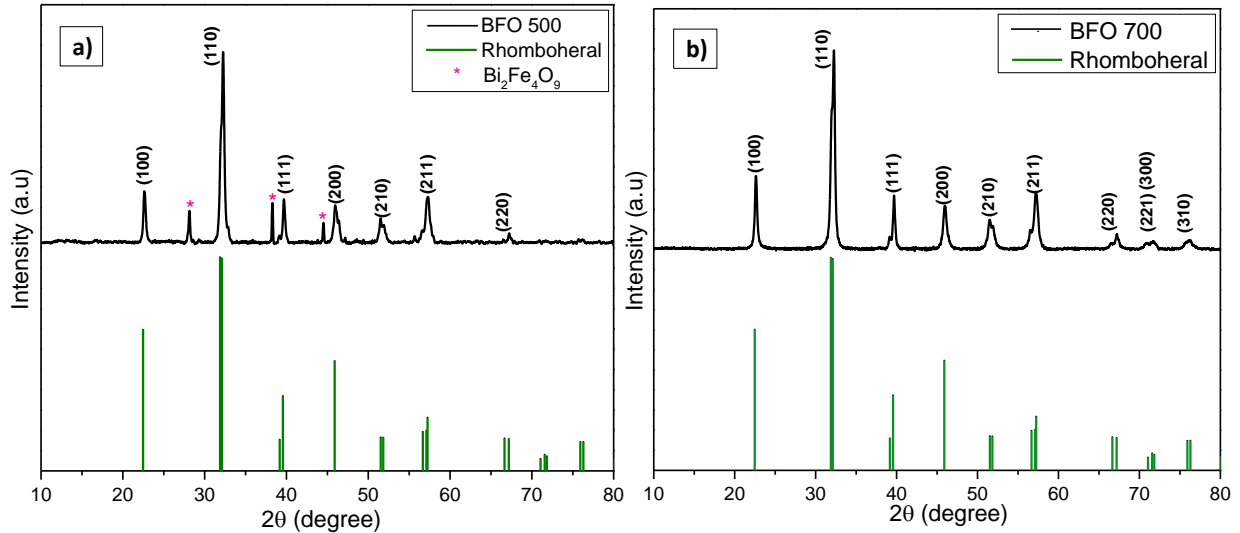


Figure 3.7: XRD of BFO a) BFO 500, annealed in air b) BFO 700, annealed in argon atmosphere

3.3.2 Structure

The XRD analysis results shown in Figure 3.7 indicate that both BFO 500 and BFO 700 have rhombohedral crystal structure which is consistent with the literature data (JCPDS card No. 01-072-2112). The pattern for BFO 500 shows weak peaks from the impurity phase $\text{Bi}_2\text{Fe}_4\text{O}_9$ which forms due to excess oxygen. When the samples were annealed at higher temperature 700°C but in absence of oxygen (argon atmosphere), the pure BiFeO_3 with distorted rhombohedral structure (space group $R3m$) was formed showing no peaks of any other impurity phases. It is well known that synthesis of pure phase BFO formation is difficult since it forms more stable $\text{Bi}_2\text{Fe}_4\text{O}_9$ phase with excess oxygen. However the impurity phase formation can be controlled by choosing appropriate synthesis conditions, which evident from present results. The average grain size calculated for BFO 500 is 20 nm and for BFO 700 is 28 nm.

Raman

The Raman analysis of the BFO 700 which is phase pure with rhombohedral crystal structure is shown in Figure 3.8 (a). The obtained spectra in analyzed and fitted with 9 individual components (3A+ 5E) and the modes of the corresponding peaks are listed in table 3.4. The table includes the comparison between the spectral signature obtained for the BFO NFs and reported data for BFO nanoparticle^[38], which are comparable to each other. As per the literature the lower frequency modes below 162 cm⁻¹ are due to the Bi atom, Fe atom usually show their signature peaks in the range of 152-261 cm⁻¹ but also some at higher frequency and mode that are above 262 cm⁻¹ are due to Oxygen atoms^[39]. The present sample shows peaks in all specified regions without any extra peak of any impurity indicates the formation of phase pure BFO that supports the XRD data.

Table 3.4: Reported Raman modes and experimental values for BFO 700 NFs

BFO Fibers (Rhombohedral)		
Reported ^[38]	Modes	Present Study
70	E1	-
125	E2	111
142	A₁ -1	-
162	A₁ -2	157
211	A₁ -3	210
236	E3	-
298	E4	270
360	E5	320
406	E6	364
469	A₁ -4	482
535	E7	-
573	E8	-
605	E9	604
-	-	750.9

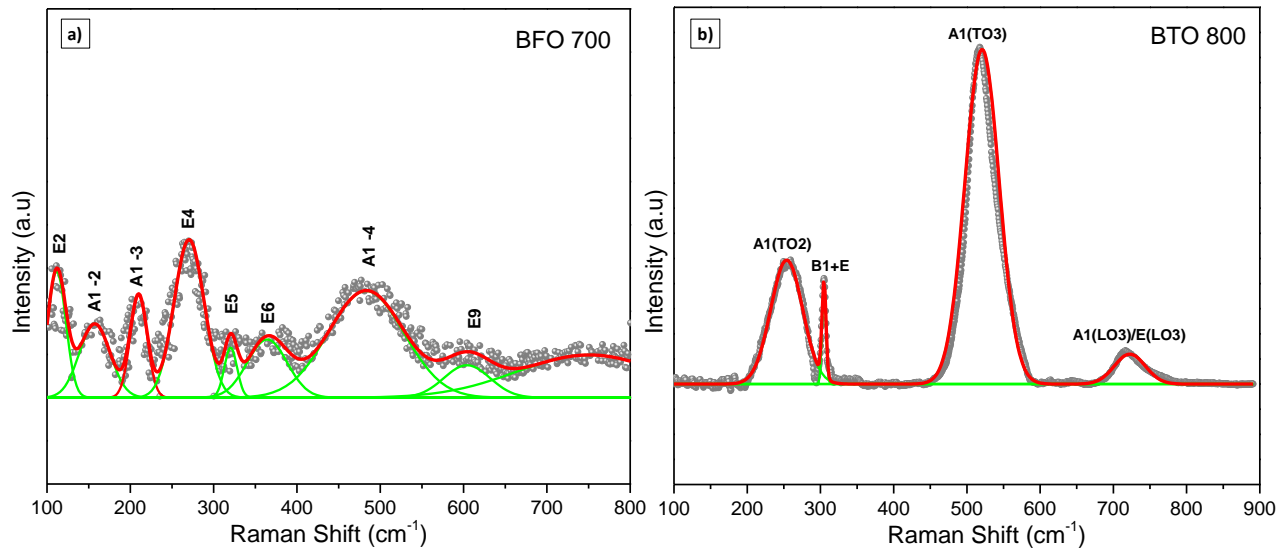


Figure 3.8: Raman spectra (a) BFO 700 NF (b) BTO 800 NF

3.4 BaTiO₃ Nanofibers (BTO NF)

3.4.1 Morphology

Figure 3.9 shows the SEM images of BTO NFs at different heat treatments. The as-spun dried BTO fibers with polymer is given in Fig 3.9 (a) and it shown a uniform surface morphology. The annealed fibers BTO 750 (Figure 3.9 (b)) and BTO (Figure 3.9 (c)) show microstructure morphology with nanometer sized grains self assembled to form tube like structure. But in BTO 750 instead of nanoparticle as grains nanoflakes are arranged to form fibers which resulted in an average diameter of 500 nm which is very large compared to BTO 800 with an average diameter of 200 nm. This concludes that the major factors that affect the surface morphology of fibers is the annealing conditions, especially temperature. The EDAX spectra and elemental mapping obtained confirms the formation of BTO maintaining 1: 1 ratio of Ba: Ti.

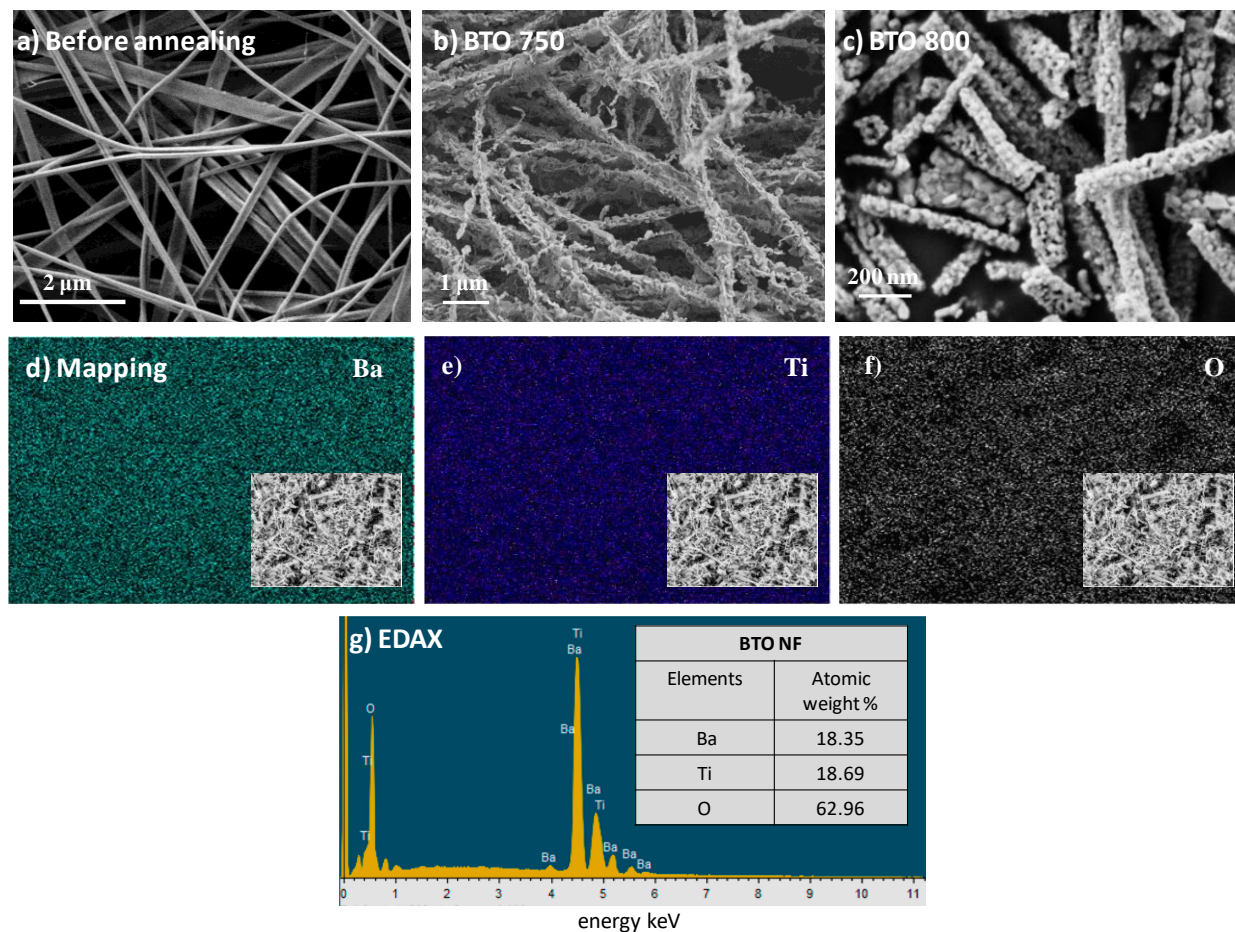


Figure 3.9: FESEM images and EDAX spectra of BTO NFs (a) before annealing (b) BTO 750 (c) BTO 800 (d) – (f) Elemental mapping (e) EDAX spectrum (inset table showing the elemental composition

3.3.2 Structure

X-ray diffraction analysis carried out to understand the phase purity and crystal structure reveals that BTO NFs are phase pure with tetragonal structure for both BTO 750 (Figure 3.10 (a)) and BTO 800 (Figure 3.10 (b)). The obtained pattern matches well with JCPDS card No: 01-074-1957 for tetragonal phase. The grain size calculated for BTO 750 is 30 nm and for BTO 800 it is 24 nm which is consistent with the values obtained from the FESEM images. The unit cell parameter calculated for tetragonal and cubic system is given in table 3.1, where the c/a ratio calculated for tetragonal system in BFO 750 turned out to be 0.9 which is smaller than bulk value 1.01 due to nanosize effect as observed in other fibers.

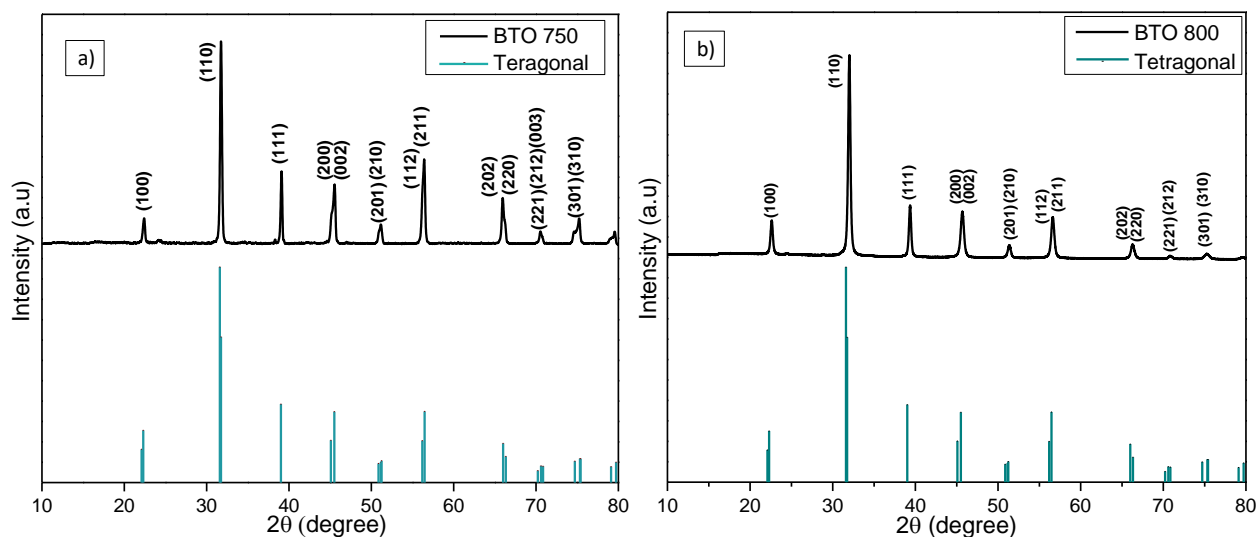


Figure 3.10: XRD pattern of BTO NFs a) BTO 750 b) BTO 800

Raman

The Raman spectra for BTO is extensively studied and it is well known that tetragonal BTO samples give four signature peaks^[40] at 250, 520 and 720 cm^{-1} which are usually broad and a sharp peak at 306 cm^{-1} . The peak at 250 and 520 cm^{-1} corresponds to the transverse optic (TO) modes of A_1 , the sharp peak at 306 cm^{-1} is due to the B_1 and E ($TO+LO$) modes and the peak at 715 cm^{-1} is from the LO modes of A_1 and E . Figure 3.8 (b) and table 3.5 (b) shows that the BTO NFs annealed at 800° C has all the above mentioned peaks of tetragonal phase.

Table 3.5 Reported Raman modes and experimental values for BTO 800 NFs

BTO Nanofiber (tetragonal)		
Reported ^[40]	Modes	Present Study
259	$A_1(\text{TO}2)$	253
306	$B_1 + E$	304
521	$A_1(\text{TO}3)$	520
715	$A_1(\text{LO}3)/ E(\text{LO}3)$	722

3.5 Composite & Heterostructure

3.5.1 FESEM

The FESEM images obtained for composite fibers before annealing and after annealing are shown in Figure 3.11 (a) and Figure 3.11 (b), (c) respectively. The fibers before annealing appears to be uniformly distributed in size with a smooth surface morphology and thus the fibers of two materials HFO and BTO are indistinguishable. The images of composite after annealing (3.11 (a) and (b)) show two distinct fibers. Comparing with the FESEM images of individual HFO and BTO, the smoother one is HFO and the other with larger diameter and coarser nature is BTO. It is also noticed that in composite, the fibers of HFO and BTO are randomly distributed without any layer formation or other complex structure formation. The elemental mapping shown in Figure 3.11 (d) – (h) confirms the presence of all elements and is quantitatively represented in table and as EDAX spectrum (Figure 3.11 (i)).

Figure 3.12 represents the FESEM data obtained for the heterostructure of HFO and BTO. The image of fibers before annealing (Figure 3.12 (a)) indicates that the fibers are uniformly distributed and they are not distinct. The images of fibers post heat treatment given in Figure 3.12 (b) & (c) confirms the heterostructure formation showing three different layers with BTO sandwiched between HFO. The fibers appears to the rough because of the heat treatment but not broken and thus retaining the fiber nature and high aspect ratio. The elemental mapping shows the presence of all the elements indicating that the effective amount of HFO is less compared to BTO.

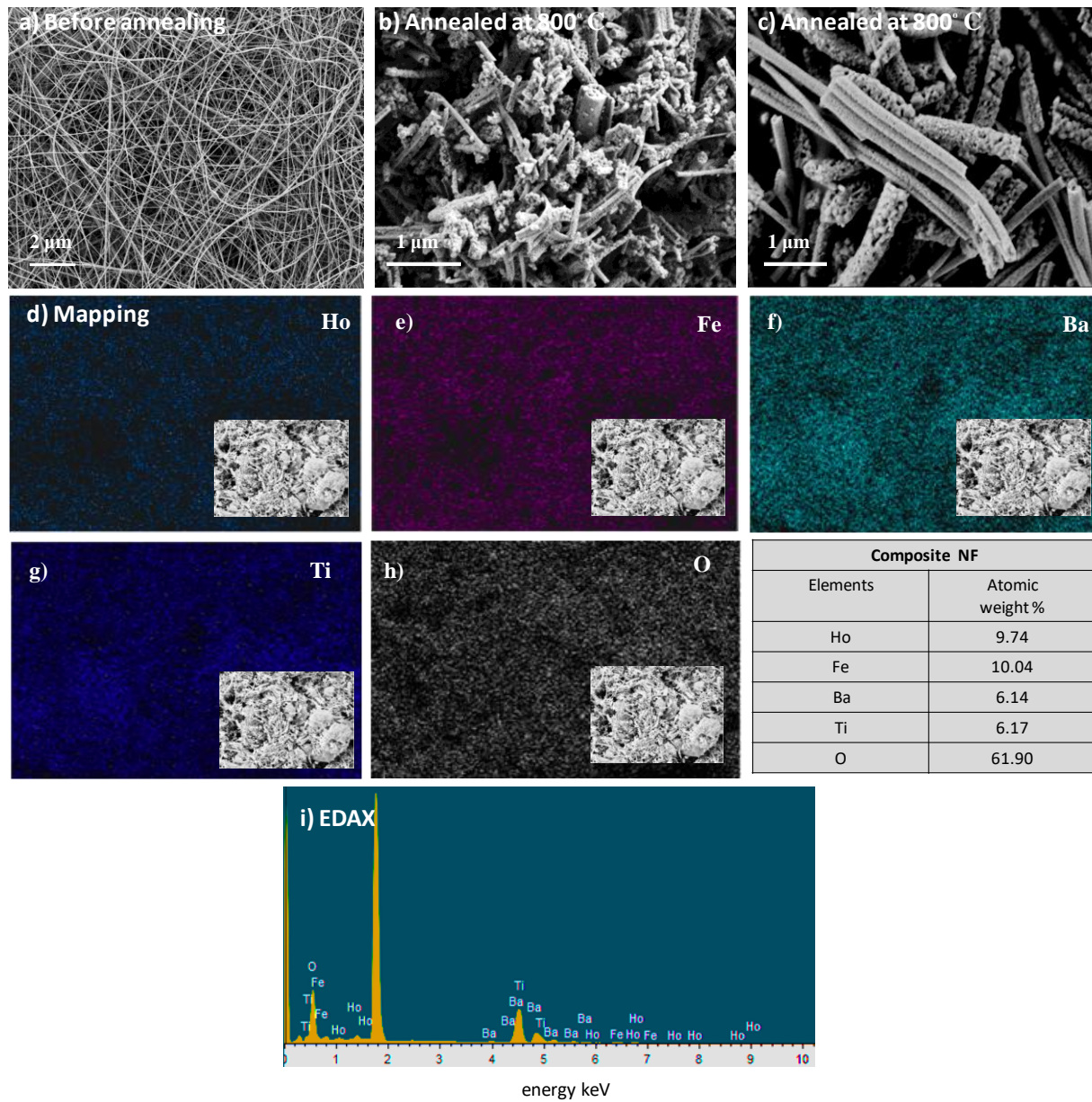


Figure 3.11: FESEM images and EDAX spectra of Composite (a) before annealing (b) – (c) after annealing (d) – (h) Elemental mapping (i) EDAX spectrum (table shows the composition of elements)

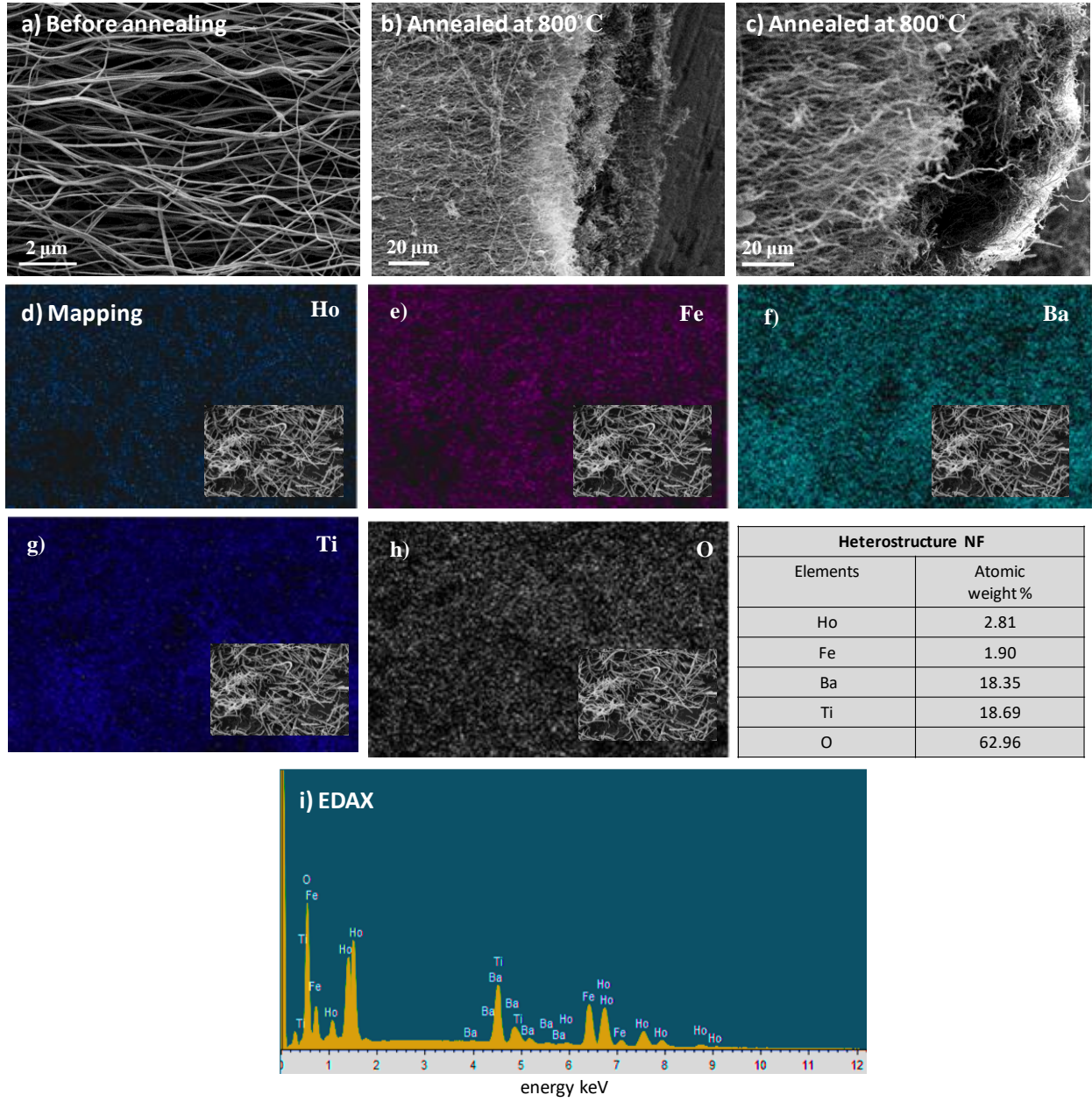


Figure 3.12: FESEM images and EDAX spectra of Heterostructure (a) before annealing (b) – (c) after annealing (d) – (h) Elemental mapping (i) EDAX spectrum (table shows the composition of elements)

3.5.2 XRD

The structure analysis for both composite and heterostructure carried out by XRD is shown in Figure 3.13 along with prepared HFO and BTO samples. The XRD pattern obtained for both composite and heterostructure confirms the presence of two phases: orthorhombic of HFO and tetragonal of BTO. In both the samples it is observed that the BTO diffraction peaks are broader than HFO peaks indicating the smaller grain of BTO fibers in composite and heterostructure. A closer look into the XRD reveals that the BTO peaks are more prominent compared to HFO peaks in both composite and heterostructure, thus the effective amount of BTO is larger than HFO present. Comparing the individual composition of HFO and BTO in composite and heterostructure, it is observed that the relative amount of HFO is less in heterostructure than composite which is in agreement with EDAX results. Here it is worth mentioning that the structural difference within the composite/heterostructure as well as the difference in the quantitative composition of the two fibers within the composite/heterostructure will contribute to impact their physical properties.

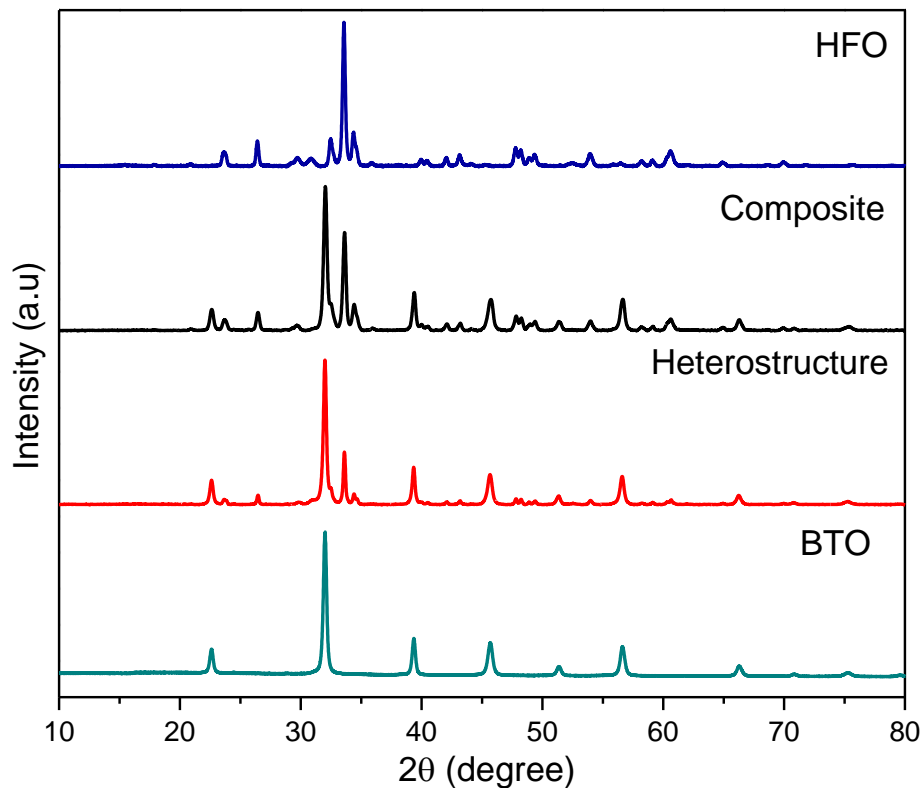


Figure 3.13 XRD pattern of composite and heterostructure

Rietveld Refinement

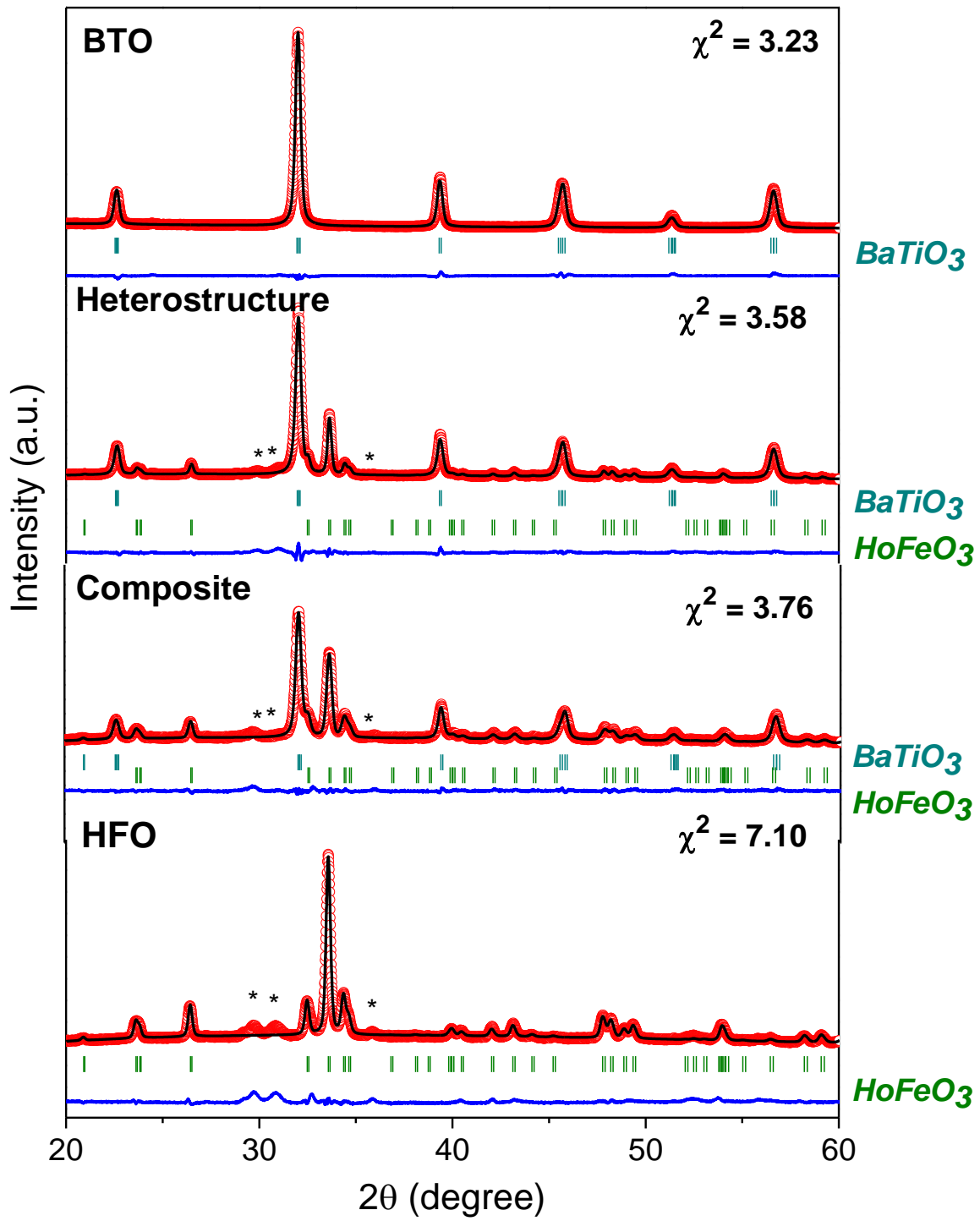


Figure 3.14 Refinement results for composite and heterostructure

The rietveld refinement results obtained for HFO, BTO, composite and heterostructure nanofibers are presented in Figure 3.14. It confirms the phase purity of each sample with corresponding crystal structure. HFO NFs have orthorhombic structure and BTO NFs have tetragonal structure, which is usually the ferroelectric phase. The composite fibers show the presence of both parent compounds with BTO and HFO in 54% and 46% respectively. The heterostructure nanofibers made by sandwiching BTO between HFO shows the presence of both the phases with small impurity of Ho_2O_3 which is also observed in HFO fibers. From refinement results the percentage composition of BTO and HFO turned out to be 70.7% and 29.3% respectively.

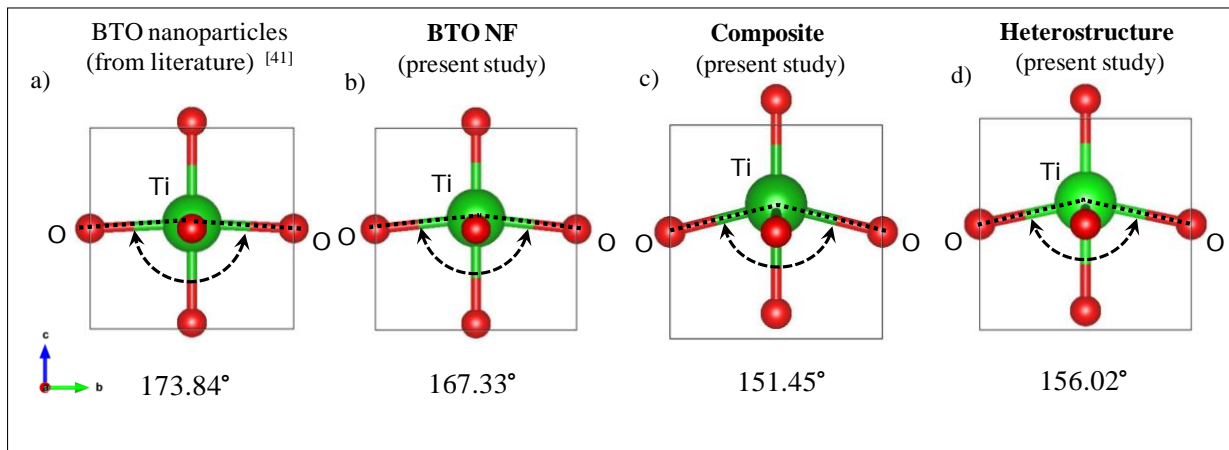


Figure 3.15 Distortion of TiO_6 octahedra

The TiO_6 octahedra model for BTO structure deduced from refinement parameters are given in Figure 3.15 (b), (c) and (d) for BTO NFs, composite and heterostructure respectively along with a reported results of BTO nanoparticle^[41] (Figure 3.15 (a)). It is observed that, compared to BTO NFs the inplane O-Ti-O angle shows a decrease in composite and heterostructure NFs due to the shifting of Ti from the inversion center. The values obtained from the present study (BTO, composite and heterostructure NFs) are smaller compared to the reported value in BTO nanoparticle. The distortion in TiO_6 octahedra will cause broken symmetry and hence a possibility of increase in the ferroelectric polarization (the ferroelectric origin in BTO is displacement from symmetry). In addition to that, an increase in average (Fe-O-Fe) angle in composite (143.35°) and heterostructure (141.68°) when compared to uncoupled HFO (139.7°) is

also observed. The change in angle brings distortion to the system that could affect the exchange coupling and change the magnetic properties (yet to be studied).

3.5.3 Raman

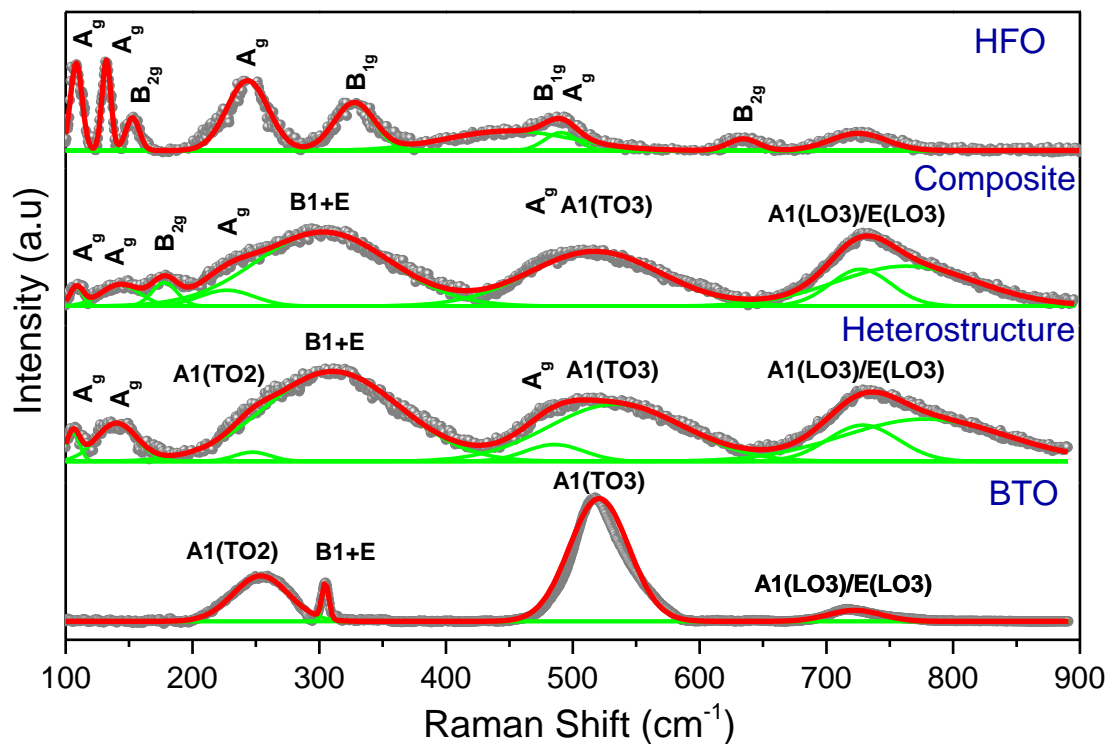


Figure 3.16 Raman spectrum of composite and heterostructure

The Raman spectrum obtained for the composite and heterostructure is shown in Figure 3.14. The experimentally obtained Raman modes of composite and heterostructure are presented along with HFO and BTO in Table 3.6; it is explicit that both the composite and heterostructure show the signature peaks of HFO and BTO. The deconvoluted Raman spectrum shows that in composite five peaks corresponding to different modes of HFO are present with three peaks of BTO. Whereas in heterostructure all the four peaks of BTO with five peaks of HFO is observed. The presented data confirms the presence of both parent compounds in the prepared materials and is corroborated with the XRD results.

Table 3.6 Raman data of composite and heterostructure compared with HFO and BTO

Present Study : Composite & Heterostructure			
HFO (H)	Composite	Heterostructure	BTO (B)
108	108 – H	105.8 – H	-
132	143 – H	139.9 – H	-
152	177 – H	-	-
237	227 – H	-	-
243	-	-	-
-	-	247 – B	253
-	303 – B	310 – B	304
449	-	485 – H	-
490	517 – H, B	-	520
-	-	534 – H	-
634	-	-	-
725	727 – H, B	728 – H, B	722
-	762	777	-

3.5.4 Physical property measurement

a) M – H loop measurements

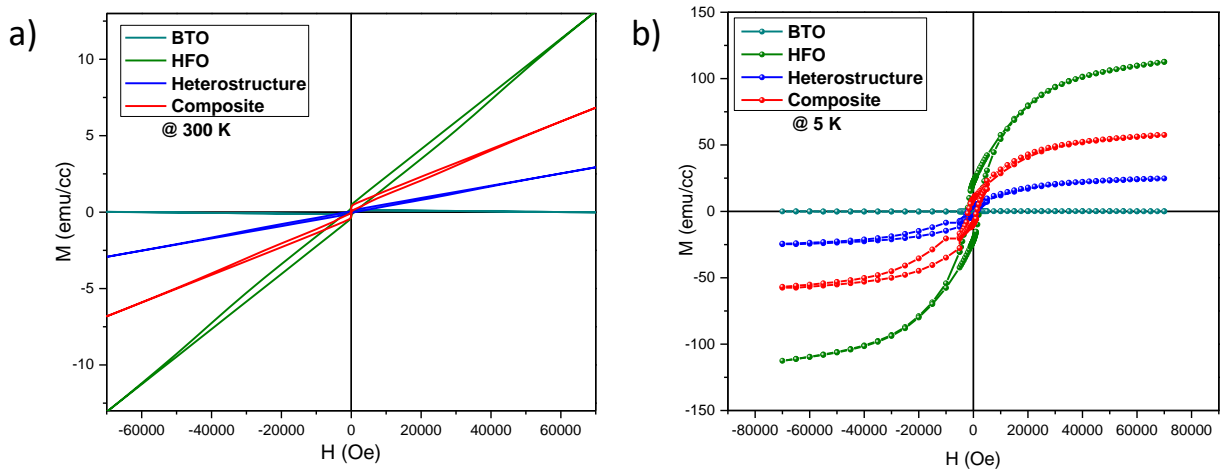


Figure 3.17: a) M-H loop of HFO, BTO, composite and heterostructure obtained at 300 K b) M – H loop of HFO, BTO, composite and heterostructure at 5 K

The M – H loops obtained for HFO, BTO, composite and heterostructure at room temperature (300 K) and at low temperature (5 K) are given in Figure 3.17 (a) and (b) respectively. The room temperature measurements reveal that HFO shows magnetic hysteresis as expected, since it contains Ho ion with highest magnetic moment of 10 μ B. And BTO, which is a ferroelectric material, do not show any response to the applied magnetic field, which is also expected. The composite and heterostructure containing both HFO and BTO shows a magnetic behavior arising from the HFO NFs. Nanocomposite which contain more percentage composition of HFO (70%) than in heterostructure (54%) shows higher saturation magnetization (M_S) values, but both lesser than HFO. This decrease in saturation magnetization (M_S) is attributed to the presence of BTO. The M-H curves obtained at 5 K (Figure 3.17 (b)) shows higher M_S values for all the samples because of decrease in thermal agitations on the spin of electrons.

b) P – E loop measurements

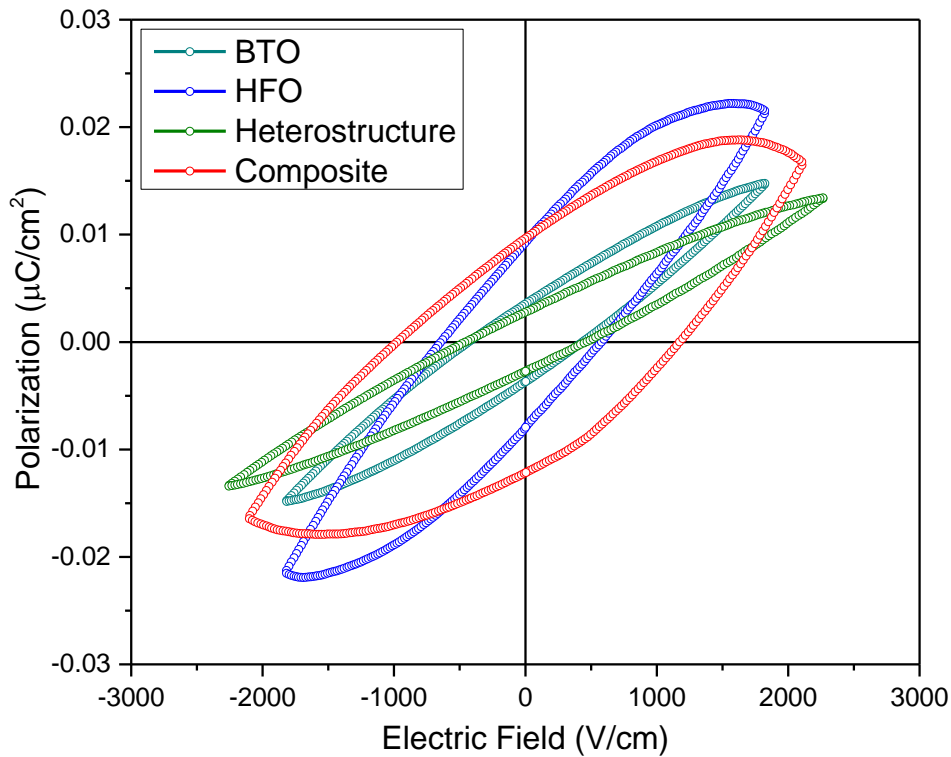


Figure 3.18: P – E loop for HFO, BTO, composite and Heterostructure

Figure 3.18 shows the P – E loop obtained for HFO, BTO, composite and Heterostructure. It is observed that BTO and Heterostructure shows ferroelectric behaviour and hysteresis is traced. HFO and composite shows poor ferroelectric characteristics with a lossy loop, because of the leakage current components from HFO. However the similar characteristics obtained for BTO and heterostructure (having 70% BTO) is interesting.

3.6 Concluding Remarks

Nanofibers of two rare earth orthoferrites LuFeO_3 & HoFeO_3 , Bismuth ferrite BiFeO_3 – a room temperature multiferroics and Barium Titanate BaTiO_3 – a well known ferroelectric material successfully synthesized by versatile electrospinning technique. The prepared samples exhibited distinct and well defined morphology with high aspect ratio as observed from FESEM images and the phase purity of the samples were confirmed by XRD. Different annealing temperature required to obtain fibers showed that the structure and morphology of the samples are temperature dependent. The structure and morphology are confirmed seen in XRD and FESEM results. Among the prepared fibers HoFeO_3 with Ho having highest magnetic moment were chosen as the magnetic parent compound and made composite with BaTiO_3 . Electrospinning technique was employed to make composite and heterostructure of HFO and BTO so that the fiber morphology is maintained within the heterostructure as well.

The morphology of composite and heterostructure were observed by FESEM. In composites after annealing two distinct fibers of HFO and BTO were seen and in heterostructure the layered arrangement is explicit. The compositional analysis carried out by EDAX showed the presence of all expected elements in appropriate proportion. The XRD analysis confirmed the presence of two structures, orthorhombic of HFO and tetragonal of BTO, which was also confirmed by deconvoluted Raman spectra. The prepared samples are robust and reproducible, showing the signatures of both parent compounds. The composite holds the possibility to demonstrate multiferroicity and / or magnetoelectric coupling.

The observed distortions in TiO_6 octahedra and increase in Fe-O-Fe angle in composite and heterostructure is very interesting. The M-H loop and P-E loop confirms the presence of magnetic and electric properties of composite and heterostructure.

Chapter 4

Summary and future direction

4.1 What was achieved?

Magnetoelectric Multiferroics is an active area of research where all the work is focused to achieve multiferroicity in materials. The presence of two primary orders will increase the degree of freedom available for a material from two to four and thus promising for technological applications. The present world with advance technological system requires faster data storage and data transfer with low energy consumption and there lies the importance of multiferroic materials. Such materials with coexistence of magnetic and electric ordering have four states for memory storage and the data can be written electrically and read magnetically, with low energy consumption. The chemical incompatibility for the existence of two orders makes the single phase multiferroics rare in nature. In this scenario nanocomposite approach to couple a magnetic and an electric material attracted the scientific community and it is promising. Nanocompositing brings the property of two parent compounds in the same materials and induces strain mediated coupling between them.

The present work focuses on synthesizing a material with the coexistence of two ferroic orders with coupling between them. Nanofibers of two rare earth orthoferrites LuFeO_3 and HoFeO_3 were synthesized along with BiFeO_3 using electrospinning technique. Among them HFO was selected as the magnetic parent and made composite and heterostructure with BTO. All the prepared fibers were characterized using FESEM and EDAX for morphological and compositional studies. XRD and Raman were employed for the structural studies and confirmed the phase purity of all the samples. The XRD and Raman of composite and heterostructure showed that both the samples have signatures of parent compounds HFO and BTO. The refinement results obtained for composite reveals that the compositions of BTO and HFO to be 54% and 46% respectively and in heterostructure the compositions of BTO and HFO to be 70% and 30% respectively. The distortion of TiO_6 octahedra in BTO and O-Fe-O angle in HFO in heterostructure nanofibers compared to uncoupled fibers indicates the effect of incorporation of one material with other. The preliminary characterization with M – H loop and P – E loop gives

an idea that ferroelectric and magnetic ordering is incorporated in the present studied system (composite and heterostructure).

4.2 What next?

The P – E loops obtained are poor in nature because of the lossy component from the HFO. So it has to be considered irrational for the confirmation of ferroelectric behaviour even though it is sufficient as a preliminary measurement. Advanced studies like magneto dielectric measurements have to be conducted to confirm the coupling effect between the two orders present.

Bibliography

- [1] Wang, J.; Neaton, J. B.; Zheng, H.; Nagarajan, V.; Ogale, S. B.; Liu, B.; Viehland, D.; Vaithyanathan, V.; Schlom, D. G.; Waghmare, U. V.; Spaldin, N. A.; Rabe, K. M.; Wuttig, M.; Ramesh, R. Epitaxial BiFeO₃ Multiferroic Thin Film Heterostructures. *Science* (80-.). **2003**, 299 (5613), 1719–1722.
- [2] LandauLifshitz-ElectrodynamicsOfContinuousMedia.pdf.
- [3] Astrov, D. N. The Magnetoelectric Effect in Antiferromagnets. *Sov. Phys. JETP* **1960**, 11 (3), 708–709.
- [4] Hill, N. a. Why Are There so Few Magnetic Ferroelectrics? *J. Phys. Chem. B* **2000**, 104 (29), 6694–6709.
- [5] Van Aken, B. B.; Palstra, T. T. M.; Filippetti, A.; Spaldin, N. A. The Origin of Ferroelectricity in Magnetoelectric YMnO₃. *Nat. Mater.* **2004**, 3 (3), 164–170.
- [6] Kimura, T.; Goto, T.; Shintani, H.; Ishizaka, K.; Arima, T.; Tokura, Y. Magnetic Control of Ferroelectric Polarization. *Nature* **2003**, 426 (6962), 55–58.
- [7] Tokunaga, Y.; Furukawa, N.; Sakai, H.; Taguchi, Y.; Arima, T.; Tokura, Y. Composite Domain Walls in a Multiferroic Perovskite Ferrite. *Nat. Mater.* **2009**, 8 (7), 558–562.
- [8] Schmid, H. Multi-Ferroic Magnetoelectrics. *Ferroelectrics* **1994**, 162 (1), 317–338.
- [9] Khomskii, D. Classifying Multiferroics: Mechanisms and Effects. *Physics (College. Park. Md).* **2009**, 2, 20.
- [10] Martin, L. W.; Ramesh, R. Multiferroic and Magnetoelectric Heterostructures. *Acta Mater.* **2012**, 60 (6–7), 2449–2470.
- [11] Taylor, P. Access Details : Access Details : [Subscription Number 777306420] On Definitions , Units , Measurements , Tensor Forms of the Linear Magnetoelectric Effect and on a New Dynamic Method Applied to Cr-Cl Boracite TENSOR FORMS OF THE LINEAR MAGNETOELECTRIC . **2010**, No. 777306420, 37–41.

- [12] Scott, J. F. Data Storage: Multiferroic Memories. *Nat. Mater.* **2007**, *6* (4), 256–257.
- [13] Nan, C. W.; Bichurin, M. I.; Dong, S.; Viehland, D.; Srinivasan, G. Multiferroic Magnetolectric Composites: Historical Perspective, Status, and Future Directions. *J. Appl. Phys.* **2008**, *103* (3).
- [14] Vopson, M. M. Fundamentals of Multiferroic Materials and Their Possible Applications. *Crit. Rev. Solid State Mater. Sci.* **2015**, *40* (4), 223–250.
- [15] Nan, C. W. Magnetolectric Effect in Composites of Piezoelectric and Piezomagnetic Phases. *Phys. Rev. B* **1994**, *50* (9), 6082–6088.
- [16] Fiebig, M. Revival of the Magnetolectric Effect. *J. Phys. D. Appl. Phys.* **2005**, *38* (8).
- [17] Hu, S.; Chen, L.; Wu, Y.; Yu, L.; Zhao, X.; Cao, S.; Zhang, J.; Ren, W. Selected Multiferroic Perovskite Oxides Containing Rare Earth and Transition Metal Elements. *Chinese Sci. Bull.* **2014**, *59* (36), 5170–5179.
- [18] Bharathkumar, S.; Sakar, M.; K., R. V.; Balakumar, S. Versatility of Electrospinning in the Fabrication of Fibrous Mat and Mesh Nanostructures of Bismuth Ferrite (BiFeO_3) and Their Magnetic and Photocatalytic Activities. *Phys. Chem. Chem. Phys.* **2015**, *17* (27), 17745–17754.
- [19] Lu, R. E.; Chang, K. G.; Fu, B.; Shen, Y. J.; Xu, M. W.; Yang, S.; Song, X. P.; Liu, M.; Yang, Y. D. Magnetic Properties of Different CoFe_2O_4 Nanostructures: Nanofibers versus Nanoparticles. *J. Mater. Chem. C* **2014**, *2* (40), 8578–8584.
- [20] Zhou, M.; Yang, H.; Xian, T.; Ma, J. Y.; Zhang, H. M.; Feng, W. J.; Wei, Z. Q.; Jiang, J. L. Morphology-Controlled Synthesis of Orthorhombic LuFeO_3 Particles via a Hydrothermal Route. *J. Alloys Compd.* **2014**, *617*, 855–862.
- [21] Chowdhury, U.; Goswami, S.; Bhattacharya, D.; Ghosh, J.; Basu, S.; Neogi, S. Room Temperature Multiferroicity in Orthorhombic LuFeO_3 . *Appl. Phys. Lett.* **2014**, *105* (5).
- [22] Wang, W.; Zhao, J.; Wang, W.; Gai, Z.; Balke, N.; Chi, M.; Lee, H. N.; Tian, W.; Zhu, L.; Cheng, X.; Keavney, D. J.; Yi, J.; Ward, T. Z.; Snijders, P. C.; Christen, H. M.; Wu, W.;

- Shen, J.; Xu, X. Room-Temperature Multiferroic Hexagonal LuFeO₃ Films. *Phys. Rev. Lett.* **2013**, *110* (23), 1–5.
- [23] Zhu, Q.; Xie, Y.; Zhang, J.; Liu, Y.; Zhan, Q.; Miao, H.; Xie, S. Multiferroic CoFe₂O₄–BiFeO₃ Core–shell Nanofibers and Their Nanoscale Magnetoelectric Coupling. *J. Mater. Res.* **2014**, *29* (5), 657–664.
- [24] You, S.; Liu, C.; Liu, H.; Yu, X.; Li, S.; Liu, W.; Guo, S.; Zhao, X. The Preparation and Characterization of 1D Multiferroic BFO/P(VDF-TrFE) Composite Nanofibers Using Electrospinning. *Mater. Lett.* **2014**, *130*, 157–159.
- [25] Jong-Han, S.; Joong-Hee, N.; Jung-Ho, C.; Byung-Ik, K.; Myoungpyo, C.; Duck-Kyun, C. Microstructures and Multiferroic Properties of Electrospun BiFeO₃ Nanofibers. *J. Korean Phys. Soc.* **2011**, *59* (3), 2308.
- [26] Wang, W.; Li, N.; Chi, Y.; Li, Y.; Yan, W.; Li, X.; Shao, C. Electrospinning of Magnetical Bismuth Ferrite Nanofibers with Photocatalytic Activity. *Ceram. Int.* **2013**, *39* (4), 3511–3518.
- [27] Nanofibres, C. B.; Feng, Y.; Wang, H.; Shen, Y.; Lin, Y.; Nan, C.; Al, E. T. Magnetic and Photocatalytic Behaviors of Ca Mn Co-Doped BiFeO₃ Nanofibres. *Mod. Res. Catal.* **2013**, *2* (3), 1.
- [28] Smith, M. B.; Page, K.; Siegrist, T.; Redmond, P. L.; Walter, E. C.; Seshadri, R.; Brus, L. E.; Steigerwald, M. L. Crystal Structure and the Paraelectric-to-Ferroelectric Phase Transition of Nanoscale BaTiO₃. *J. Am. Chem. Soc.* **2008**, *130* (22), 6955–6963.
- [29] Kolezyński, A.; Tkacz-Śmiech, K. From the Molecular Picture to the Band Structure of Cubic and Tetragonal Barium Titanate. *Ferroelectrics* **2005**, *314* (October 2014), 123–134.
- [30] Bhardwaj, N.; Kundu, S. C. Electrospinning: A Fascinating Fiber Fabrication Technique. *Biotechnol. Adv.* **2010**, *28* (3), 325–347.
- [31] Lee, W. Y.; Yun, H. J.; Yoon, J. W. Characterization and Magnetic Properties of LaFeO₃ Nanofibers Synthesized by Electrospinning. *J. Alloys Compd.* **2014**, *583* (3), 320–324.

- [32] Yuh, J.; Nino, J. C.; Sigmund, W. M. Synthesis of Barium Titanate (BaTiO₃) Nanofibers via Electrospinning. *Mater. Lett.* **2005**, *59* (28), 3645–3647.
- [33] Kulkarni, S. K. *Nanotechnology : Principles and Practices*.
- [34] Chaturvedi, S.; Shyam, P.; Apte, A.; Kumar, J.; Bhattacharyya, A.; Awasthi, A. M.; Kulkarni, S. Dynamics of Electron Density, Spin-Phonon Coupling, and Dielectric Properties of SmFeO₃ Nanoparticles at the Spin-Reorientation Temperature: Role of Exchange Striction. *Phys. Rev. B* **2016**, *93* (17), 1–12.
- [35] Venugopalan, S.; Becker, M. M. Raman Scattering Study of LuFeO₃. *J. Chem. Phys.* **1990**, *93* (6), 3833–3836.
- [36] Suresh, P.; Laxmi, K. V.; Kumar, P. S. A. Synthesis and Structural Properties of Hexagonal-LuFeO₃ Nanoparticles. **2016**, 20472, 20472.
- [37] Venugopalan, S.; Dutta, M.; Ramdas, A. K.; J. P. Remeika. Rare-Earth Orthoferrites: *Phys. Rev. B - Condens. Matter Mater. Phys.* **1985**, *31* (3), 1490–1497.
- [38] Chaturvedi, S.; Bag, R.; Sathe, V.; Kulkarni, S.; Singh, S. Holmium Induced Enhanced Functionality at Room Temperature and Structural Phase Transition at High Temperature in Bismuth Ferrite Nanoparticles. *J. Mater. Chem. C* **2016**, *4* (4), 780–792.
- [39] Hermet, P.; Goffinet, M.; Kreisel, J.; Ghosez, P. Raman and Infrared Spectra of Multiferroic Bismuth Ferrite from First Principles. *Phys. Rev. B - Condens. Matter Mater. Phys.* **2007**, *75* (22), 3–6.
- [40] Badapanda, T.; Senthil, V.; Panigrahi, S.; Anwar, S. Diffuse Phase Transition Behavior of Dysprosium Doped Barium Titanate Ceramic. *J. Electroceramics* **2013**, *31* (1–2), 55–60.
- [41] Yashima, M.; Hoshina, T.; Ishimura, D.; Kobayashi, S.; Nakamura, W.; Tsurumi, T.; Wada, S. Size Effect on the Crystal Structure of Barium Titanate Nanoparticles. *J. Appl. Phys.* **2005**, *98* (1).